Dancing with the Electrons: Time-Domain and CW *In Vivo* EPR Imaging

Sankaran Subramanian and Murali C. Krishna

Radiation Biology Branch, Center for Cancer Research, National Cancer Institute, National Institutes of Health, Bethesda, MD 20892, U.S.A.

Abstract: The progress in the development of imaging the distribution of unpaired electrons in living systems and the functional and the potential diagnostic dimensions of such an imaging process, using Electron Paramagnetic Resonance Imaging (EPRI), is traced from its origins with emphasis on our own work. The importance of EPR imaging stems from the fact that many paramagnetic probes show oxygen dependent spectral broadening. Assessment of *in vivo* oxygen concentration is an important factor in radiation oncology in treatment-planning and monitoring treatment-outcome. The emergence of narrow-line trairylmethyl based, bio-compatible spin probes has enabled the development of radiofrequency time-domain EPRI. Spectral information in time-domain EPRI can be achieved by generating a time sequence of T_2* or T_2 weighted images. Progress in CW imaging has led to the use of rotating gradients, more recently rapid scan with direct detection, and a combination of all the three. Very low field MRI employing Dynamic Nuclear polarization (Overhauser effect) is also employed for monitoring tumor hypoxia, and re-oxygenation *in vivo*. We have also been working on the co-registration of MRI and time domain EPRI on mouse tumor models at 300 MHz using a specially designed resonator assembly. The mapping of the unpaired electron distribution and unraveling the spectral characteristics by using magnetic resonance in presence of stationary and rotating gradients in indeed 'dancing with the (*unpaired*) electrons', metaphorically speaking.

Keywords: EPR imaging, magnetic resonance, single point imaging, *in vivo* oxymetry, time-domain, pulse EPR, overhauser MRI

Introduction

Magnetic resonance spectroscopy, in general, deals with the precessional frequency of magnetic nuclei, such as ^{1}H, ^{13}C, ^{19}F, ^{31}P, etc. and that of unpaired electrons in free radicals and systems with one or more unpaired electrons when placed in a uniform magnetic field. The phenomena of nuclear induction and electron resonance were discovered more or less at the same time, (Bloch, Hansen and Packard, 1946; Purcell, Torrey and Pound, 1946; Zavoisky, 1945) and have become two of the most widely practiced spectroscopic techniques. The finite dimensional spin space of magnetic nuclei makes it possible to quantum mechanically precisely predict how the nuclear spin systems will behave in a magnetic field in presence of radiofrequency fields. On the other hand, the complex and rather diffuse wave functions of the unpaired electron which get further influenced by the magnetic vector potential make it a real challenge to predict the precise behavior of electron resonance systems. The subtle variations in the precessional frequencies brought about by changes in the electronic environment of the magnetic nuclei in NMR and that of the unpaired electrons in EPR make the two techniques widely practiced and very useful in the structural elucidation of complex biomolecules (Emsley and Feeney, 1965; Field, Sternhill and Sternhill, 1989; Weil, Bolton and Wetz, 1994). It was discovered subsequently (Lauterbur, 1973, 1986) that the presence of linear field gradients enabled precise spatial registration of nuclear spins which led to the development of imaging of the distribution of magnetic nuclei establishing an important non-invasive medical imaging modality of water-rich soft tissues in living systems with its naturally abundant presence of protons (Haacke, Brown, Thompson et al. 1999; Mitchell and Cohen, 2003). Nuclear Magnetic Resonance Imaging, popularly known as MRI, is now a well-known and indispensable tool in diagnostic radiology. Apart from being one of the most widely used clinical imaging tool, MRI finds important applications in investigating dynamics (perfusion and diffusion of aqueous components), angiography, blood volume, brain function (BOLD, Blood Oxygen Level MRI), *in vivo* biochemistry (spectroscopic imaging), etc. (Moonen, Bandettini, Aquirre et al. 1999; Ogawa, Tank,

---

Correspondence: Sankaran Subramanian, Radiation Biology Branch, CCR, NCI, National Institutes of Health Building 10, Room B3B69 9000 Rockville Pike Bethesda 20892. Tel: (301) 443 6490; Email: subu@helix.nih.gov

Menon et al. 1992). MRI started with early imaging modalities involving field or frequency sweep for spectral measurements in presence of static gradients and images were derived using projection-reconstruction techniques (Lauterbur and Lai, 1980; Lauterbur, Levin and Marr, 1984). With the development of pulsed excitation, Fourier transform methods and pulsed field gradients, it became possible to perform slice selective excitation and obtain sophisticated images with image contrast controlled by different aspects of the dynamics of the spin system that can be very selectively studied by a variety of tailored schemes of pulses and gradients. In addition, spectroscopic imaging with volume selective excitation provides important non-invasive biochemical information. Apart from application to life sciences, MR imaging has been developed to investigate solid state materials and, in addition, to perform microscopy in suitable systems as well (Callaghan, 1993).

The entirely analogous field of electron paramagnetic (spin) resonance (EPR or ESR) that deals with unpaired electron systems developed as a structural tool much more rapidly with the intricate spectra of free radicals and metal complexes providing an abundance of precise structural information on molecules, that would otherwise be impossible to unravel. The spectroscopic practice of EPR traditionally started in the microwave region of the electromagnetic spectrum and was essentially a physicist's tool to study magnetic properties and the structure of paramagnetic solid state materials, crystal defects (color centers), etc. Later, chemists started using EPR to unravel the structure of organic free radicals and paramagnetic transition metal and lanthanide complexes. Early EPR instrumentation closely followed the development of radar systems during the Second World War and was operating in the X-band region of the electromagnetic spectrum (~9 GHz) (Ingram, 1955; Poole, 1997). Pulsed EPR methods developed somewhat later due to the requirement of ultra fast switches and electronic data acquisition systems that can cope with three orders of magnitude faster dynamics of the electrons, compared to that of protons (Kevan and Bowman, 1990; Schweiger and Jeschke, 2001). The absence of relatively long-lived free radicals of detectable range of concentration in living systems made *in vivo* EPR imaging not practical. It became essential that one has to introduce relatively stable biocompatible free radicals as probes into the living system in order to image their distribution. Further the commonly practiced X-band EPR frequency is not useful for interrogating reasonable size of aqueous systems due lack of penetration. Frequencies below L-band (1–2 GHz) are needed for sufficient penetration and one has to employ either water soluble spin probes that can be introduced into the living system (via intramuscular or intravenous infusion) or solid particulate free radicals that can be implanted *in vivo*. Early imaging attempts were entirely in the CW mode at L-band frequencies (1–2 GHz) on small objects. For addressing objects such a laboratory mouse, rat etc., it became necessary to lower the frequency down to radiofrequency (200–500 MHz). With CW EPR imaging, the imaging approach is one of generating projections in presence of static field gradients and reconstructing the image via filtered back-projection as in X-ray CT or positron emission tomography (PET) (Brownell, Budinger, Lauterbur et al. 1982; Kak and Slaney, 1988). Most spin probes used for small animal *in vivo* imaging get metabolically and/or renally cleared within a short time and hence there is need to speed up the imaging process. Further, the very fast dynamics, with relaxation times on the order of microseconds of common stable spin probes such as nitroxides, until recently, precluded the use of pulsed methods that are in vogue in MRI.

The early practice of *in vivo* CW EPRI was at L-band with low frequency modulation and phase sensitive detection. Images were reconstructed using spatial encoding under constant gradients at different orientations to generate projections followed by filtered back projection (Berliner and Fujii, 1985; Eaton, Eaton and Ohno, 1991). By making measurements at a set of gradients and re-sampling the projections one can generate an additional spectral dimension that will lead to the estimate of spatially resolved spectral parameters and hence add functionality to images (Eaton, Eaton and Maltempo, 1989; Maltempo, Eaton and Eaton, 1987). This slow process is often not able to compete with the fast pharmacokinetic and renal elimination of the spin probe and hence faster imaging methods were needed. By lowering the frequency to 300 MHz, and by using ultra narrow line spin probes based on the triarylmethyl (TAM) radicals (Ardenkjaer-Larsen, Laursen, Leunbach et al. 1998), the National Cancer Institute developed time-domain EPR imaging methods which provided images much faster (Subramanian, Matsumoto, Mitchell et al. 2004; Subramanian, Murugesan, Devasahayam et al. 1999; Subramanian, Yamada, Irie et al. 2002a). Further developments in the time-domain EPR imaging involved the use of constant-time or single point imaging (*vide infra*) involving pure phase-encoding that generated images with improved resolution (Subramanian, Devasahayam, Murugesan et al. 2002b). T_2* weighted contrast in the single point imaging mode could be used to quantitatively assess *in vivo* oxygen levels (Subramanian et al. 2002a). Simultaneously T_2 weighted imaging using the well-known spin echo (90°-τ-180°) pulse sequence followed by the FT of the echo and filtered back-projection proved to be yet another alternative quantitative oxymetry procedure. (Mailer, Subramanian, Pelizzari et al. 2006) In the meanwhile, CW imaging approaches also were being modified for improved temporal resolution. The importance of the CW approach is that it is not limited exclusively to the narrow line spin probes. An increase in imaging speed was achieved using a stepped-field with fast rotating gradients, (Ohno and Watanabe, 2000; Deng, He, Petryakov et al. 2004) The detection was still with low frequency modulation that imposes an upper limit on the field scan speed. A more recent development involves the use of direct detection of resonances without low frequency modulation that will allow arbitrary rapidscan of the field. At high speeds, rapid scan will generate 'ringing' that can be removed by cross correlation (Joshi, Ballard, Rinard et al. 2005; Stoner, Szymanski, Eaton et al. 2004). Finally, to our knowledge, the fastest CW imaging to date is by a combination of rapidscan, rotating gradients and direct-detection (vide infra) (Subramanian, Koscielniak, Devasahayam et al. 2007).

Another very closely related imaging modality which also employs unpaired electrons is PEDRI (Proton Electron Double Resonance Imaging) (Lurie, Bussell, Bell et al. 1988) or OMRI (Overhauser-enhanced Magnetic Resonance Imaging) (Golman, Leunbach, Ardenkjaer-Larsen et al. 1998; Golman et al. 1998; Golman, Leunbach, Petersson et al. 2002) developed recently that utilizes the Overhauser effect. Protons are polarized in the presence of stable free radicals to provide highly enhanced MR images at very low fields. The principle behind OMRI is the saturation of a free radical EPR resonance by continuous (or pulsed) irradiation at the electron resonance frequency, which leads to an Overhauser enhancement of the proton magnetization (also known as Dynamic Nuclear Polarization, DNP) *via* time-dependent dipolar interactions between the unpaired electrons and the water protons. Under ideal conditions and 100% saturation this would lead to an enhancement factor of 329 ($0.5 \times \gamma_{\mathrm{elctron}}/\gamma_{\mathrm{proton}}$). Since the electronic magnetic moment is 658 times higher than of the proton one needs fields on the order of only 10 mT. At this field the electron resonance frequency is ~300 MHz and that of protons is around 0.5 MHz corresponding to very low field MRI. The enhancement factor depends on the *in situ* line width of the paramagnetic spin probe, which is influenced, apart from local dynamics, remarkably and quantitatively by the local oxygen concentration. This technique has been used to non-invasively and quantitatively assess *in vivo* pO_2, at very low fields with good sensitivity. OMRI produces images of good quality and resolution (Golman, Petersson, Ardenkjaer-Larsen et al. 2000; Krishna, English, Yamada et al. 2002).

It is also possible to perform EPRI co-registered with MRI without moving the subject from the resonator in between the measurements. This leads to a better correlation of anatomical and functional parameters derived from both imaging modalities and can prove to be of improved clinical relevance.

In what follows, we describe, albeit briefly, the progress in the EPR imaging field with particular reference to our own work at the National Cancer Institute. In a review such as this it is difficult to cover exhaustively all the work published in the field. An excellent monograph by Eaton et al. (Eaton, Eaton and Ohno, 1991) and three volumes of the series in Biological Magnetic Resonance, together, cover most of the progress made in this field till 2005 (Berliner 2003; Eaton, Eaton and Berliner, 2005a; Eaton, Eaton and Berliner, 2005b).

CW EPR Imaging

Instrumentation

There are excellent descriptions of the CW EPR instrumentation in the literature (Eaton, Eaton and Ohno, 1991; Ingram, 1955; Poole, 1997) and only a brief description is given here. The essential parts of a CW EPR imaging spectrometer are (a) a radiation source (traditionally in the microwave regime of the electromagnetic spectrum, but at frequencies at and below L-band for *in vivo* EPRI),

(b) a microwave (or an RF) bridge, a circulator (directional coupler or magic-T) that isolates the transmit and detector arms of the bridge, and a diode detector; (c) a resonant cavity (usually of the reflection type) or coil (LC circuit) to store the energy and house the object to be imaged: (d) a stable DC magnetic field with good homogeneity and sweep capability; (e) a modulation unit that can sinusoidally modulate the DC field at frequencies of a few tens of kHz. (f) signal receiver consisting of a lock-in amplifier and phase sensitive detector; (g) for performing imaging, additionally we require a set of three mutually orthogonal gradient coils with the associated computer controlled bipolar power supplies; and finally, (h) a computer for automation and ease of complete operation of the spectrometer/imager.

Although EPR spectroscopy can be performed at any frequency, based on considerations of frequency-dependent sensitivity and penetration as well as the dielectric and magnetic permittivity of biological objects (tissue, nerve, etc.), for imaging fair-sized biological objects, frequency in the range 250–500 MHz is the best compromise in terms of sensitivity and penetration. The spectrometer should have a provision for additional feedback regulatory circuits for automatic frequency control (AFC), and/or automatic coupling/matching controls(AMC/ACC) (Brivati, Stevens and Symons, 1991; Hirata and Fujii, 2007; Hirata and Luo, 2001; Hirata, Walczak and Swartz, 1997) to correct for thermal drifts of the static magnetic fields and to keep the matching and tuning of the resonator during animal motion (*via* heart-beat and peristalsis). It is also important to have the volume occupied by the animal thermostatically controlled at the physiological temperature of the animal.

For imaging, the sample or animal is placed in the resonator, positioned in the center of the static magnetic field, tuned and matched to the radiation source. When there is an impedance match between the cavity and the source arm of the bridge, the radiation will exist as standing waves and there will be no reflection of microwave/RF power from the cavity corresponding to the so-called *critical coupling* condition. Resonant cavities are characterized by the quality factor Q which is a measure of the ratio between the stored energy and the energy dissipated per cycle of radiation. When resonance condition (a match between the precessional frequency of the electrons and that of the source frequency) is satisfied, the impedance gets altered, and the coupling is no longer critical. This leads to a reflection of a small amount of power, which reaches the diode detector via the circulator. A phase sensitive detection scheme is used to enhance the sensitivity of the spectrometer. In this scheme, the DC magnetic field is modulated sinusoidally at a low frequency in the range 10–100 kHz. This leads to an amplitude modulation of the signal reflected from the resonator at the modulation frequency, with the amplitude of detected signal being proportional to the slope of the absorption signal. In the signal channel, all signals with phases and frequencies different from the modulation frequency and phase are removed. The narrower the bandwidth of the receiver filter, better would be the relative signal to noise ratio (SNR). Such a phase sensitive detection largely eliminates noise from the detection diodes, and baseline artifacts due to drifts in the DC electronics and makes such a detection scheme very efficient. The schematics of our home-built 300 MHz CW spectrometer, complete description of the sub-assemblies, operation and the sensitivity of the spectrometer have already been reported. (Koscielniak, Devasahayam, Moni et al. 2000).

Because of the relatively large line widths of common spin probes used in EPR, CW methods were preferred for EPRI. Several research groups have also developed resonators, and excellent *in vivo* EPR instrumentation for CW EPRI (Alecci, Dellapenna, Sotgui et al. 1992; Halpern, Spencer, van Polen et al. 1989). Such studies have provided valuable information on the pO_2 (partial pressure of oxygen) levels in tumors. CW L-band imaging studies have also provided information on cardiac ischemia and tumors (Kuppusamy, Chzhan, Vij et al. 1994; Matsumoto, Thirumaran, Chandrika et al. 2003; Zweier, Wang and Kuppusamy, 1995). However, because of the relatively longer times taken for projection data acquisition, imaging times are long (several minutes to hours depending on the dimensionality of the image), often requiring continuous infusion of the spin probe, to offset for metabolic and pharmacokinetic elimination of the probe from the system. To minimize artifacts associated with cardiac motion during imaging experiments one has to resort to appropriate gating techniques.(Kuppusamy, Chzhan, Wang et al. 1996a).

Common resonators used in MRI, such as solenoidal, saddle, surface coils, birdcage etc., are equally suitable for CW EPRI. All resonators are series LC circuits or parallel LC circuits with the resonance frequency given by $\omega_0 = (1/2\pi)\,(LC).^{-0.5}$ The resonators are characterized by their quality factor Q and the conversion efficiency defined as the amplitude of the oscillatory magnetic field per square root of electrical energy (Watts) applied. The quality factor, Q, can be defined as 2π times the ratio of the energy stored in the resonator to that dissipated per cycle. It should be noted that for a conventional resonance circuit with C in parallel with a series combination of L and R, the quality factor is given by $(\omega_0\, L)/R$, whereas for a parallel combination of L and R it is given by $R/(\omega_0\, L)$. Q can also be defined as the ratio of resonance frequency divided by resonator band width. Therefore, high Q resonators have narrow bandwidth and concomitant higher amplitude of oscillatory magnetic field at the resonance frequency (higher conversion efficiency), while low Q resonators have larger frequency bandwidth and lower amplitude of magnetic field at resonance frequency. High Q resonators are to be preferred in CW EPR spectroscopy and imaging because of the narrow detection bandwidth, but low Q resonators are the only choice in time-domain EPRI. For low frequency EPRI, the loop-gap resonator, (Froncisz and Hyde, 1982) re-entrant cavity resonator, (Chzhan, Kuppusamy, Samouilov et al. 1999) and parallel-coil resonators (Devasahayam, Subramanian, Murugesan et al. 2000) are in common use. Another novel device is the truncated transmission line used as a broadband resonator (Rubinson, Cook, Mitchell et al. 1998). For the sake of topical or localized imaging of larger objects which need not be enclosed in a volume resonator, surface coils of various designs have also been developed for *in vivo* EPR (Alecci, Brivati, Placidi et al. 1998; Froncisz, Oles and Hyde, 1989; Hirata, Walczak and Swartz, 2001; Hyde, Froncisz and Oles, 1989; Ono, Ogata, Hsieh et al. 1986; Pfenninger, Forrer, Schweiger et al. 1988; Rinard, Quine and Eaton, 2000; Sakamoto, Hirata and Ono, 1995).

Air core and iron core magnets operating up to L-band frequencies with homogeneities better than 100 ppm have been constructed (Quine, Rinard, Eaton et al. 2002) and are also commercially available. There is no need for the incorporation of magnetic field shims that are standard in NMR and MRI. The homogeneity of the main magnetic field is an important determinant in resolution achievable in an imaging context. The maximum tolerated magnetic field inhomogeneity will depend on the line width of the spin probes used in the imaging experiments. For imaging with nitrosyl spin probes and spin labels, it is enough if the magnetic field inhomogeneity is much less than the line width of the probe. This is because, in order to spatially resolve two points separated by a distance d, the gradient magnitude G (T/m) should be such that d × G should exceed the line width. Since EPR measurements up to L-band uses fields of about 40 mT (400 Gauss), and the line widths of normal spin labels are around 0.1 mT, homogeneity of ~200 ppm is more than adequate. However, when one uses special spin probes such as triarylmethyl derivatives, which have line widths in the range 4 to 20 μT, much better homogeneity over the volume of interest would be required.

A three axes gradient coil system is used for spatial encoding of the spin distribution. These gradients are powered by computer controlled bipolar power supplies with current regulation. The required maximum gradients will depend on the object size, the line width of the spin probe and the resolution sought in the image. For getting mm resolution using nitrosyl radicals (with an assumed line width of 0.1–0.2 mT) spin probes for imaging objects such as a mouse, gradient strengths in excess of 200 mT/m are required. For higher resolution one has to use water-cooled high power gradient coils. Usually Maxwell coils (coaxial with the Zeeman field) are used for the z-gradient, and two pairs each of saddle coils are used for generating the x- and y-gradients. Water-cooled gradient coil systems delivering up to 1.2 T/m are available (Kuppusamy et al. 1994). Gradient coils for EPR imaging are also commercially available. The gradient linearity should be better than 1%. The gradient settling time is not very critical for CW EPR, since all spatial encoding experiments use stationary gradients and relatively slow sweeps of the static field. It is, however, important in some modes of time-domain EPR.

Spin probes for EPR imaging

As already mentioned, unlike MRI, EPR imaging requires the introduction of paramagnetic spin probes into the subject. The desired qualities of spin probes useful for EPR imaging at radio frequency for *in vivo* applications, are as follows (for time-domain EPR imaging, the EPR line width of the spin probe should be narrow, preferably less than 20 μT, such that its time-domain response at RF survives beyond the spectrometer recovery time (vide infra). For CW EPRI, there is no restriction on the line width):

a) The spin probe should have single line EPR spectra, since, for imaging applications, all the spatial information can be provided by a single line. A probe with multi-line EPR spectrum will have redundant information, and reduced sensitivity.
b) The *in vivo* stability of the paramagnetic spin probe should be such that its half-life is longer than 10–15 minutes to permit 3-D image data collection.
c) The spin probe should be water-soluble such that the probe can be administered either intravenously or intraperitoneally with toxicity of the spin probe being minimal at the doses required for EPR imaging.
d) In addition, if the line width varies with pO_2, it will permit the estimation of *in vivo* tissue oxygen concentration from the EPR image data.

The spin probes we have employed for both CW and time-domain imaging and oxygen mapping are stable paramagnetic species, which are non-toxic, and water-soluble, based on the tri-aryl methyl (TAM) skeleton. The structural details of these agents and their EPR properties are described elsewhere (Ardenkjaer-Larsen et al. 1998). Recently these spin probes with a single narrow EPR resonance have been evaluated as contrast agents for dynamic *in vivo* oxymetry using Overhauser enhanced MR imaging (Golman et al. 1998). Two analogs of TAM, abbreviated as Oxo31 and Oxo63 were used in our studies. The structure of these agents, their abbreviations and molecular weights are given in Figure 1. The relaxation times of some of the TAM based derivatives at RF frequency range have been reported in the literature (Ardenkjaer-Larsen et al. 1998; Golman et al. 1998; Panagiotelis, Nicholson and Hutchison, 2001; Yong, Harbridge, Quine et al. 2001). Insoluble particulate spin probes such as fusinite (Gallez, Debuyst, Dejehet et al. 1998) and lithium phthalocyanine (LiPC) (Jiang, Nakashima, Liu et al. 1996; Liu, Gast, Moussavi et al. 1993) and analogous synthetic derivatives have also been used to perform localized *in vivo* spectroscopy and oximetry (Ilangovan, Li, Zweier et al. 2001, 2002; Pandian, Kim, Woodward et al. 2006; Pandian, Parinandi, Ilangovan et al. 2003). A single line EPR spectrum whose line width depends linearly on the partial pressure of oxygen characterizes these solids. These agents have to be implanted surgically into the animal at specific anatomical locations for the purpose of studying site-specific *in vivo* oxygen measurements (Swartz and Walczak, 1998). LiPc, which is a paramagnetic semiconductor, has line widths in the range 2–4 μT in the absence of oxygen and the line width has a linear dependence on oxygen concentration. Detailed discussion on the electrochemical synthesis of LiPc and its line width dependence on oxygen partial pressure has been reported (Ilangovan, Zweier and Kuppusamy, 1999, 2000b, 2000a). These probes ($<0.2\ \mu m^3$) can be chronically implanted in the muscle or other regions of interest and repeated oxygen measurements can be made *in vivo* (Liu et al. 1993).

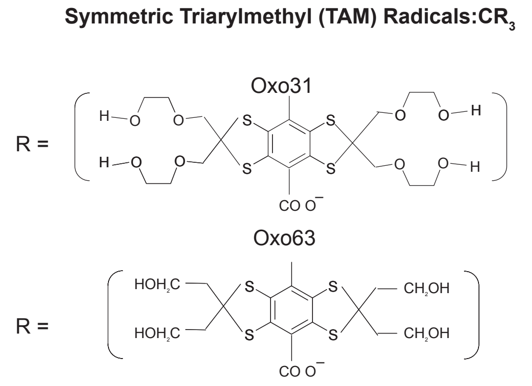

Figure 1. The molecular structure of the symmetric triarylmethyl derivatives, Oxo31 and Oxo63 used for CW and time-domain EPR imaging in our laboratory.

Image reconstruction in CW EPR

In CW EPRI, the image reconstruction follows the well-established methods of filtered back-projection techniques in X-ray CT. There is excellent literature (Bracewell, 1994; Kak and Slaney, 1988; Natterer, 1986) that describes the mathematics and practice of filtered back projection in two and three dimensions. Spectra of spin probe distribution (so-called projections) are measured in the presence of stationary gradients. Two or three-dimensional projections of an object are obtained in the presence of a stationary gradient of appropriate magnitude and orientation and acquiring the spectrum by a continuous sweep of the magnetic field to cover the complete spectral dispersion produced by the gradient. The resonance frequency encodes the spatial displacement of the spin from the origin and the amplitude at each frequency corresponds to the amount of spin at a given displacement. The resulting 'spectrum' is a one-dimensional projection image of the spin probe. A two dimensional image in the EPR sense is the complete projection of spin distribution in the object on to a selected plane. There is no simple way of 'slice selection' possible as in MRI. Information from the whole volume of spins in the object inside the resonator will contribute to the image data. For a 2D image, a vector gradient of appropriate magnitude (commensurate with line width of the paramagnetic probe and the required resolution) is applied radially at n equal intervals in steps of $\theta = \pi/n$ from 0 to $(\pi - \theta)$ and n projections are acquired. Once the number of projections and the magnitude are decided, the computer can power a set of two orthogonal gradient coils located in the 2D plane of interest and the vector gradient can be electrically rotated in the desired manner using standard vector sum methods. For 3D imaging all the three orthogonal gradients x, y and z are used and the gradient vector would span in a nested loop through equal intervals of polar and azimuthal angular increments, both covering an angular range of 0 to π, in a polar coordinate system. In other words, projections are collected in a polar raster centro-symmetric with the electrical center of gravity of the gradient axis system.

Once the projections (in two or three dimensions) have been acquired, it is straightforward to reconstruct the image using the so-called filtered back projection technique. Stated simply, the back projection performs the reverse of the operation of obtaining the projections. Each projection is smeared across in the reverse direction, which leads to a 'blurred' trans-axial image. Depending on the number of angular projections taken, this can also lead to the so-called 'star-artifacts' in the image. Applying a suitable filter to the projections before reconstruction can reduce these. The filtering is implemented by multiplying the Fourier transform of the individual projections with an appropriate filter response function and then the product is inverse Fourier transformed. The resulting filtered projections are back-projected to produce the image. The most popular filter response functions for 2D reconstruction are the Shepp-Logan (Shepp and Logan, 1974) and Ram-Lak (Ramachandran and Lakshminarayanan, 1971). The image is reconstructed from filtered projections obtained for n equally spaced angles from 0 to π (π to 2π projections will be identical since interchanging the sample and the gradient directions does not affect the projection profile) by the *discrete* approximation to the back projection integral. Because the filtered projections are in polar coordinates whereas the image is represented in Cartesian coordinates, a match between the experimental polar grid and back-projected Cartesian grid can always be approximated by linear interpolation.

Three dimensional projection reconstruction involves a two-stage reconstruction scheme (Marr, Chen and Lauterbur, 1981). The data set involving m θ-steps and m φ-steps consists of a total of m^2 projections each with, say, 128 data points. In the first stage m two dimensional planar projections are carried out from the projections each of which consisted of m projections collected with a constant azimuthal angle φ. This results in m 2D projections each with 128×128 points. Every point at the end of the first stage projection can be represented as $P(\varphi, i, j1)$, $i = 1$ to 128, $j = 1$ to 128. In the second stage all points $P(\varphi, i, j1)$, $i = 1$ to 128 are selected. These, for a given value of j, lie in planes perpendicular to the z-axis. There will be a total of 128 such sets ($j1 = 1$ to 128) which are to be back-projected resulting in a cubic array of dimension $128 \times 128 \times 128$ corresponding to the 3D image. The resulting image can be surface rendered, or cross sections can be examined using suitable 3D visualization software. For 3D back projection, one either uses a Shepp-Logan filter in each stage or a *single* second derivative filter, or the so-called three-point filter (Shepp, 1980) applied only during the first stage. In fact the second derivative filter also known as three-dimensional filter gives better results than two successive filters in each of the stages. There are a large number of iterative image processing algorithms developed for image reconstruction. Also there are several ways in which the projections data can be gathered, such as uniform distribution of solid angles over the surface of a sphere, etc.

Spectral-spatial imaging

A useful variation of the spatial imaging modality can generate what is known as a spectral-spatial image (Eaton and Eaton, 1986; Ewert and Herrling, 1986; Kuppusamy, Chzhan, Wang et al. 1996b; Lauterbur et al. 1984; Maltempo, 1986). In a standard two dimensional spatial image we have spatial dimension represented along both the axes, whereas in a 2D spectral-spatial image we will have one axis representing spatial dimension and the other representing spectral characteristics (line shape/line width etc.). Therefore, in a 2D spectral spatial image, we are confronted with a *pseudo* object, which when viewed along the so-called spatial axis contains only spatial information and when viewed along the orthogonal spectral axis contains only spectral information. In order to clearly understand the spectral spatial experimental modality (see Fig. 2), let us consider three point objects distributed along the x-axis. This axis also is the so-called spatial axis. If we now take a spectrum with no gradient applied (Fig. 2A) the spectra from all the three points will be superimposed and will appear as a single sum spectrum. (In the figure, for clarity, all the three individual spectra are shown). In the absence of gradients, we have no spatial information, and the only available spectral information is the unresolved sum of spectra from all the three sites. Let us now apply a small gradient such that the spectra from the three points just get resolved. Now we have spatial information, but the spectra are somewhat broadened due to the finite dimension of the objects (spin distribution). In other words, the individual spectral line shapes are convolved with the actual profile of the objects, corresponding to a *pseudo* projection in the spectral-spatial dimension. As we gradually increase the gradient (Figs. 2B to E) still keeping it oriented along the same axis, the spectra would span wider and wider field ranges and the profiles also will undergo additional zoom-in effect. But since we are dealing with back-projection imaging, we cannot allow the physical width of the projections to change; all spectra are, therefore, scaled so as to span identical width. Increasing the gradient further and rescaling the spectrum so that it occupies the same physical width will give a more resolved view. Therefore, as the gradient increases, the relative widths of the rescaled objects go on reducing (Figs. 2C to E), and finally with a hypothetical infinite gradient, and subsequent scaling down we should just get three delta-function profiles corresponding to only spatial information with zero-spectral information (2F). We can understand the spectral-spatial projections (2A-F) if we define a pseudo-viewing angle α given by

$$\tan(\alpha) = (\text{spatial window/spectral window}) \times \text{gradient magnitude} \qquad [1]$$

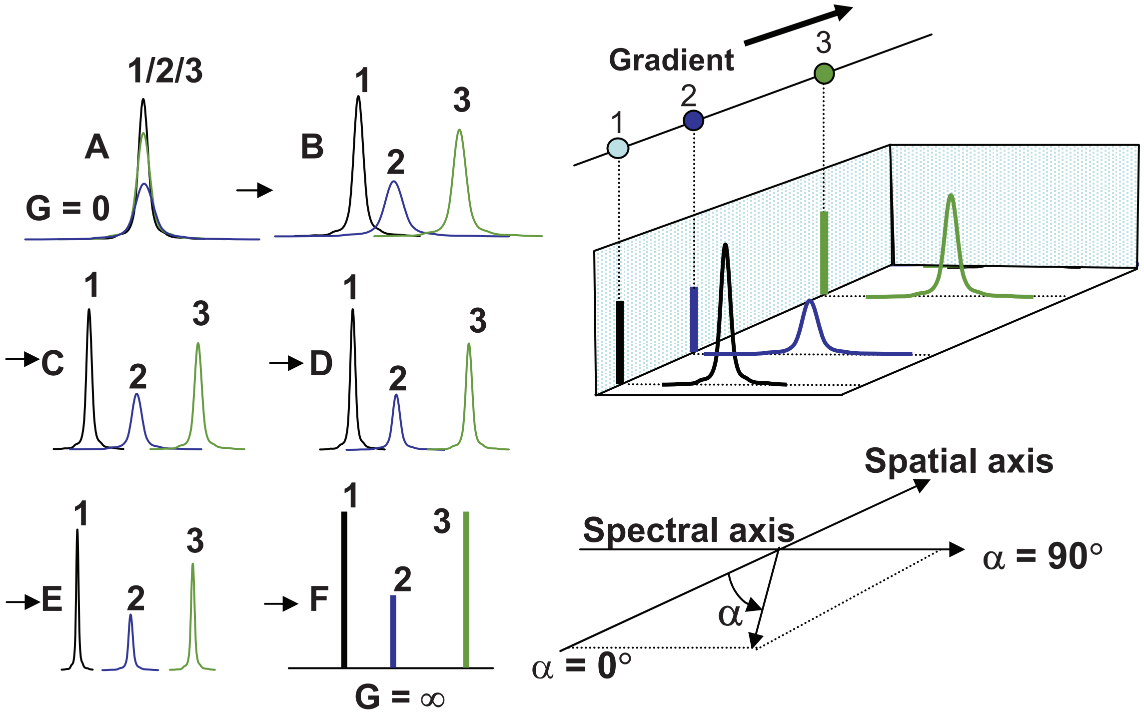

Figure 2. Concept of spectral-spatial imaging. Obtaining several sets of projections form an object with gradually increasing gradients, and rescaling the projections to same size generates views of the object in a *pseudo* spatial-spectral dimension, leading to the separation of the spectral information from the spatial information.

For a viewing angle of 90°, the corresponding gradient magnitude will be infinite and this will not be practical. A linear variation of the viewing angle will not correspond to a linear variation of the gradient, which depends rather on tan (α). The sketch on the right (Fig. 2) illustrates the back-projected image and the projections along the spectral and spatial axes (on the back and left-hand side shaded walls), which are equivalent to the projections obtained in A ($\alpha = 0°$) and F ($\alpha = 90°$). In practice, just as we collect 2D spatial profiles by rotating a constant gradient in the x–y plane in equal intervals for 180°, for a 1D-spectral-1D-spatial image we perform experiments by gradually incrementing the gradient *without* changing its direction. The gradient magnitude required can be calculated from Eqn.[1] once we have selected suitable widths for the spectral and spatial windows. For pseudo viewing angle $\alpha = 90°$ we need an infinite gradient and for α between 90° and 180° the gradient will change sign (see equation above). Since an infinite gradient is not practical, we may have to miss some profiles close to $\alpha = 90°$, but this will not adversely affect the reconstruction. One can simply perform back-projection without these projections. Missing angle back-projection algorithms are available in the literature (Maltempo, Eaton and Eaton, 1988). A 2D-spatial-1D-spectral imaging experiment will take the same time duration corresponding to a conventional 3D spatial image, and a 3D spatial and 1D spectral image will be much more time consuming. Spectral-spatial imaging has been implemented in CW EPR imaging by several researchers (Eaton, Maltempo, Stemp et al. 1987; Kuppusamy et al. 1994; Mailer, Robinson, Willimas et al. 2003) and provides pixel-wise or voxel-wise line width information that can be used to infer, say for example, the *in vivo* oxygen concentration.

Recent developments in CW EPR imaging

The relatively slow sweep rate constrained by the low frequency modulation and phase sensitive detection makes measurement of CW EPR image data collection rather time consuming. A rule of thumb for field scan rate is

$$\frac{\text{Sweep width}}{\text{Line width}} \times \frac{\text{Time Cons tan t}}{\text{Sweep Time}} < 0.1 \qquad [2]$$

It can be seen that in CW, for a sweep width in the range 1–2 mT, for probe line width in the range 0.02 to 0.1 mT and a detector time constant of 10–100 ms, the optimal sweep time is between 1 and 100 sec. For trityl radicals the sweep time for a range of 2 mT may not be less than a second to avoid line shape distortion. Such a restriction in sweep rate coupled with large number of projections to be collected for three dimensional spectral spatial imaging, and the rapid pharmacological and renal clearance of most water-soluble spin probes warrant that we have to device means of speeding up the imaging time to have reliable physiological information not compromised by rapid probe-concentration changes. Time-domain approach is an alternative (vide infra), but is not applicable to the more popular redox sensitive nitroxide probes because of the short relaxation times T_1 & T_2 (e.g. protonated nitroxides have relaxation times on the order of the resonator recovery time, <200 ns). We need, therefore, a CW imaging approach that is capable of generating image data fast enough to cope with the short pharmacokinetic and biological half-life of the spin probe. There have been a number of attempts towards this goal in CW EPR imaging, and few of the more recent attempts are outlined below.

Ohno et al. (Ohno and Watanabe, 2000) and later Deng et al. (Deng, He, Petryakov et al. 2004) suggested scanning the Zeeman field in small incremental steps and at each step rotating the gradient field vector through 360° in a plane at a low frequency and acquiring the EPR signal with a fast digitizer. At the end such a scan, one has information on all the projections that can be unraveled from the detected signal by reshuffling the data. Because the gradient rotations and the sweep are integrated, very fast scans are not needed, and yet projection information is gathered much faster than in conventional CW imaging where the gradient vector remains static throughout a given sweep. Such a procedure, which requires only changing the way in which gradient coils are powered and controlled can be easily implemented. Since the entire 2D image data can be gathered in a single field sweep. The data acquisition rate at a given field step for a full rotation (by 2π) will decide the number of projections, and the number of field steps will decide the number data points acquired per projection. It has been demonstrated that with a time constant of 10 ms, modulation amplitude of 0.05 mT, by sweeping a field interval of 1.2 mT in

64 steps (corresponding to 64 projections) and a gradient rotating frequency of 12 Hz, it was possible to acquire 2D image data in 5 sec. With the minimum speed of 2.6 sec. per scan dictated by the impedance of the magnet, it would have taken at least 166 sec. with conventional measurements with static gradients. This enables imaging times shorted by more than order of magnitude. The rotating-gradient-stepped-field schematic is shown in Figure 3.

If the limitation imposed by low frequency modulation and phase sensitive detection is removed one can use sweep rates that are arbitrarily fast. Joshi et al. and Stoner et al. have have recently published detailed accounts of performing EPR spectroscopy and imaging using *rapid scan* with *direct detection* (Joshi, Ballard, Rinard et al. 2005; Stoner, Szymanski, Eaton et al. 2004). Earlier observation of rapid scan EPR with the spectra showing the effect of transverse relaxation on the scan speed was reported by Czoch et al. in 1983 (Czoch, Duchiewicz, Francik et al. 1983). For very fast field scans, one superimposes a sinusoidal (AC) or a triangular magnetic field on the static Zeeman field by applying a suitable current to a secondary coil. Using large field amplitudes (10–20 G) at kHz frequencies one can effectively accomplish scan rates on the order of several *T*/*s* and cover the required sweep widths in times on the order of microseconds. By carefully adjusting the Zeeman filed one can make the resonances to occur in the *linear region* of a sinusoidal fast sweep, and can perform rapid scan EPR spectroscopy and imaging. With fast scans one has to use direct detection of the EPR signals. Unlike the conventional phase sensitive detection where the detection band width can be quite narrow (few kHz), the rapid field sweep will require detection bandwidth on the order of a few hundred kHz, with a concomitant reduction in signal to noise ratio. Ultra fast scan that traverses the spectral width in times on the order of transverse relaxation times will cause distortions in the spectral shape and in the limit of very fast scans produce 'ringing' at the trailing edge of the spectrum, similar to the free induction decay of spins in response to pulsed excitation. While it may not be necessary to scan at such speeds, it is quite easy to remove the ringing pattern and correct the line shape by the well-known Fourier deconvolution technique used in rapid scan correlation NMR and EPR spectroscopy (Dadok and Sprecher, 1974; Gupta, Ferretti and Becker, 1974; Joshi, Ballard, Rinard et al. 2005).

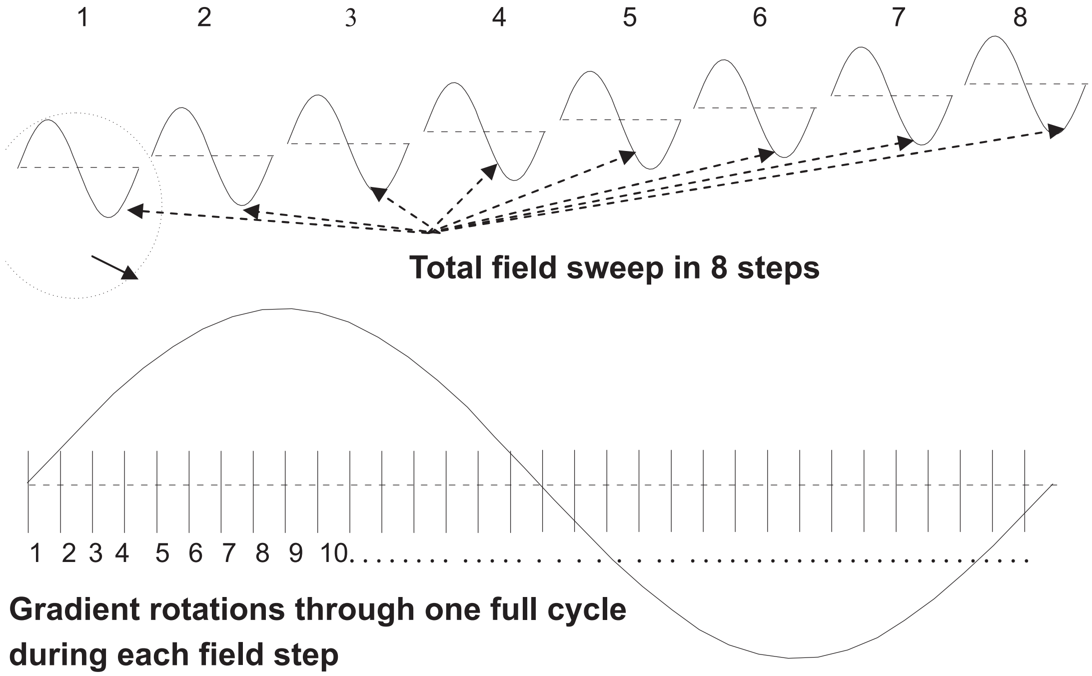

Figure 3. Simplified schematic of stepped-field and rotating gradient 2D CW EPR. The field is stepped through 8 points (top) and for each field point the gradients rotated in a plane by one full cycle. In this simplified example, the n points collected per gradient cycle are sub-sampled to 8 points to produce the Bθ matrix (Fig. 4) column-wise. By carefully adjusting the field scan rate, the gradient rotating frequency and the sampling speed one can optimize the image resolution.

A third alternative to perform rapid CW EPR imaging that we have developed is the combination of rapid scan of the magnetic field and the *simultaneous* rotation of the gradients and performing direct detection (Subramanian et al. 2007). To understand the relationship between the main strategies of fast CW EPR imaging let us consider the elements in each projection profile. For a two dimensional polar raster of the gradient, we rotate the gradient vector from an arbitrary starting angle of 0° through 180°–θ, in steps of θ. 180° to 360–θ will reproduce the projections once more. For each value of the gradient angle we collect the projections. For simplicity, let us assume that we have 8 gradient orientations (θ1 to θ8) and the projections are represented by 8 field positions (B1 to B8). The 8 projections that will result from the 2D experiment will constitute a Bθ matrix of dimension 8 × 8. Let the rows represent the field values increasing from B_{min} to B_{max} from left to right, and let the columns represent the gradient orientations from 0 to 360°–θ, in steps of (360/8)°, from top to bottom. In the conventional CW imaging mode, we follow the collection of the projections by sweeping the field at constant gradient, and then sequentially reorient the gradient vector in a polar grid through equal intervals. In other words, we determine the elements of the Bθ matrix row-wise. This is indicated by the horizontal rows in Figure 4. In rapid scan EPR imaging the imaging mode is essentially the same, except that the scan rates are very high, (and the projections may have to be subsequently processed to get rid of the FID-like ringing) and as such, here also, the Bθ matrix is collected row-wise. The vertical columns, on the other hand, correspond to filling the Bθ matrix column-wise and represent the determination of the elements by scanning the field in a stepwise fashion, with the gradients being completely rotated from 0–360°. Here the field will be incremented from start to end in a finite number of steps (eight in this simplified example) and the gradient will go from 0 to 360° in 8 θ-steps. The resulting response has to be reshuffled into conventional

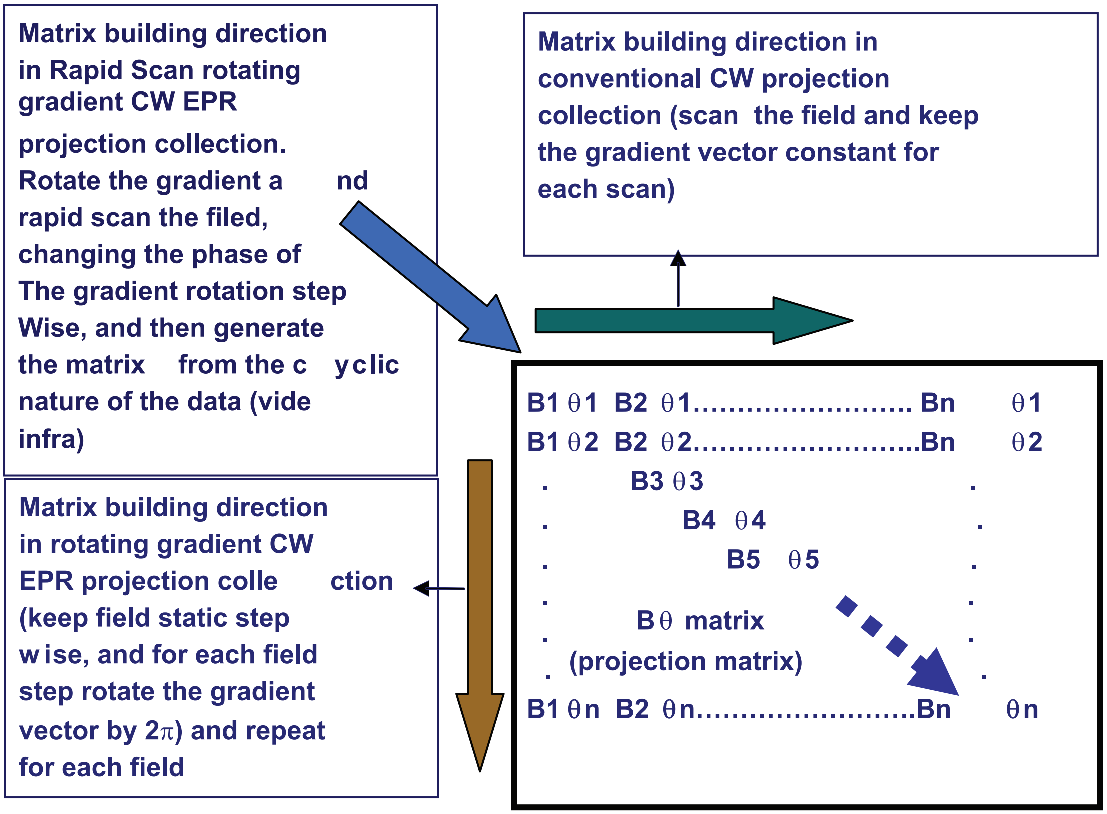

Figure 4. Elements of the Bθ matrix that represents the projections obtained at a constant gradient as a function of the orientation of the gradient vector. Elements are collected row-wise in conventional EPR imaging and column-wise in rotating-gradient stepped-field data collection. The large horizontal arrow represents the conventional way of collecting projections at constant gradient vector at a given orientation, and then changing the orientation sequentially. The big vertical arrow represents the stepped-field-rotating-gradient approach. The big slanted arrow represents the present method that corresponds to the simultaneous application of the field sweep and rotating gradients.

projections based on the total acquisition points and that for each cycle of gradient rotation, before applying filtered back-projection.

We will now examine the possibility of simultaneously scanning the field and rotating the gradients to collect the elements of the Bθ matrix, represented by the diagonal arrow direction in Fig. 4. To reduce the collection-times of projection data, we shall combine rapid scan and rotating gradients with direct detection. This would lead to absorption profiles (rather than the first derivatives obtained in phase sensitive detection). While the direct detection is less sensitive compared to phase-sensitive detection, it is partially compensated by the fact that the profile intensity in absorption mode is an order of magnitude higher than in the first derivative mode. Coming to the data collection strategy, if one looks along the diagonal of the matrix, it can be seen that both the field and the gradients monotonically increase. If we make one full sweep of the required region of the field by a rapid scan and digitize the signal in 64 or 128 steps (here it will be 8 steps) this will decide the field resolution (spatial resolution, depending on the magnitude of the gradient) and make a synchronous rotation of the gradient vector from 0–360° and the collected data will constitute the elements of the diagonal of the Bθ matrix. We can follow this by scanning the field from high to low (this will be advantageous since we do not jump from the high end of the field to the starting field abruptly, but simply perform a zigzag scan) still rotating the gradient from 0–360°. The detected signals will now fill the elements of the Bθ matrix along the anti-diagonal (right to left) from top to bottom. The other elements are to be filled along lines parallel to the diagonal or the anti-diagonal of the Bθ matrix, and in order to accomplish this we need to impart an incremental phase shift to the gradient rotation for each pair of upward and downward field scan (please see Fig. 5).

Our rapidscan-rotating gradient spectrometer (see Fig. 6 for the spectrometer schematics) works with a sinusoidal field scan frequency of 1.2 kHz, and gradient rotation frequency of 4.8 kHz.

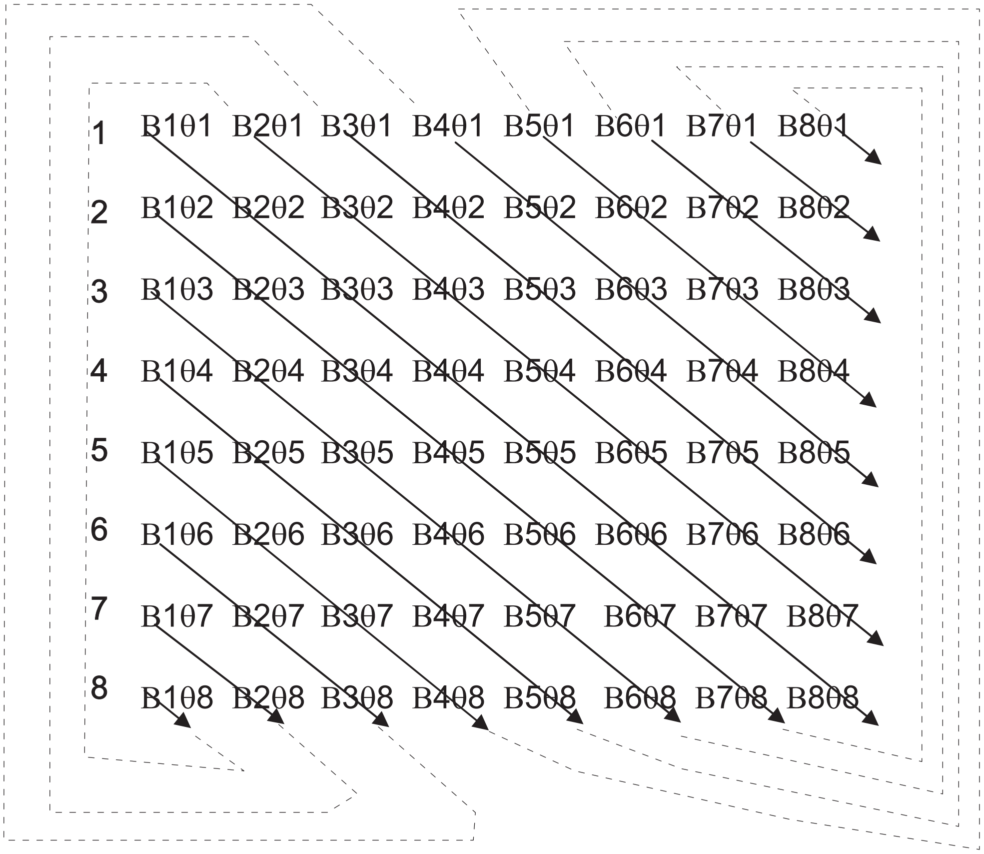

Figure 5. The Bθ projection matrix. The conventional projection data collection in presence of constant orientation of gradients is represented by the rows of the matrix. The stepped-field, rotating gradient method is represented by the columns. The simultaneous rapid-scan in presence of rotating gradients modality is represented by directions parallel to the diagonal (or anti-diagonal) of the matrix. The arrows indicate the way in which the data is collected for simultaneous sweep and gradient rotations.

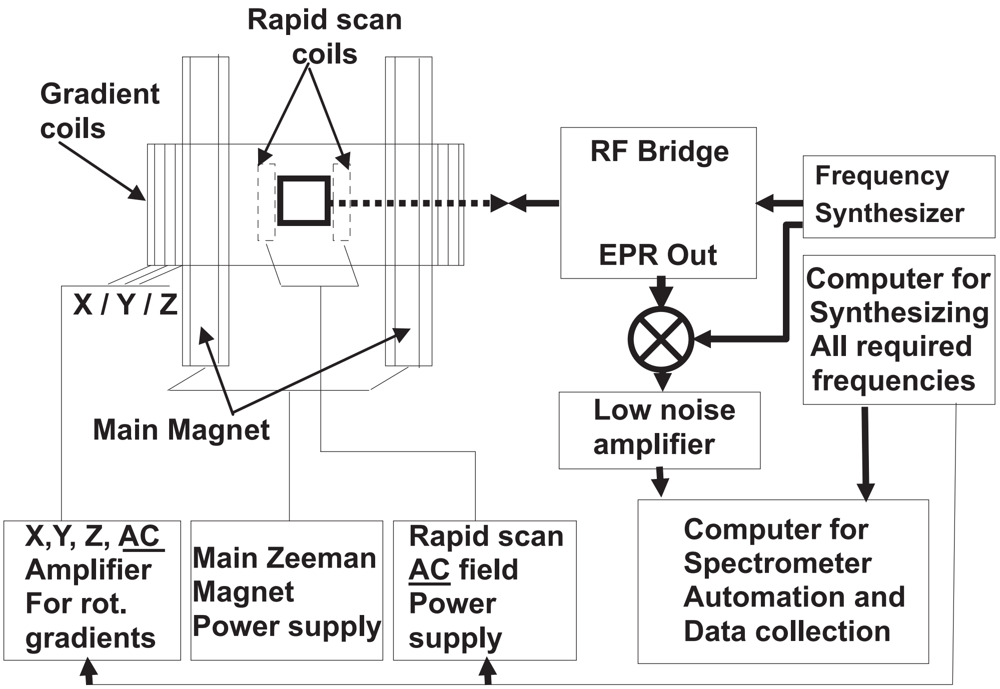

Figure 6. Simplified schematics of the Rapid scan rotating gradient CW EPR Imager.

The maximum amplitude of the field is around 2.5 mT and those of the gradients are ±40 mT/m. The relative positioning of the gradient and the sweep sinusoids allow a full cycle (2π radians) gradient rotation at the middle of the positive going and also in the negative going sweep sinusoids. The linearity within the middle 40% of the sweep sinusoid is better then 0.3% and we generate two 'pseudo' projections per sweep sinusoid. This can be repeated, and the entire signal under each full rotation of the gradient cycle is sampled in 64 (or 128) steps (Fig.7). After averaging the necessary number of pseudo projections at a constant phase of the gradients, the gradient phases are digitally shifted by 2π/64 (or 2π/128) and the collections continued. The resulting 64 × 64 (or 128 × 128) projection matrix constitutes a skewed 2D 'pseudo' sinogram, which can be unskewed by shuffling

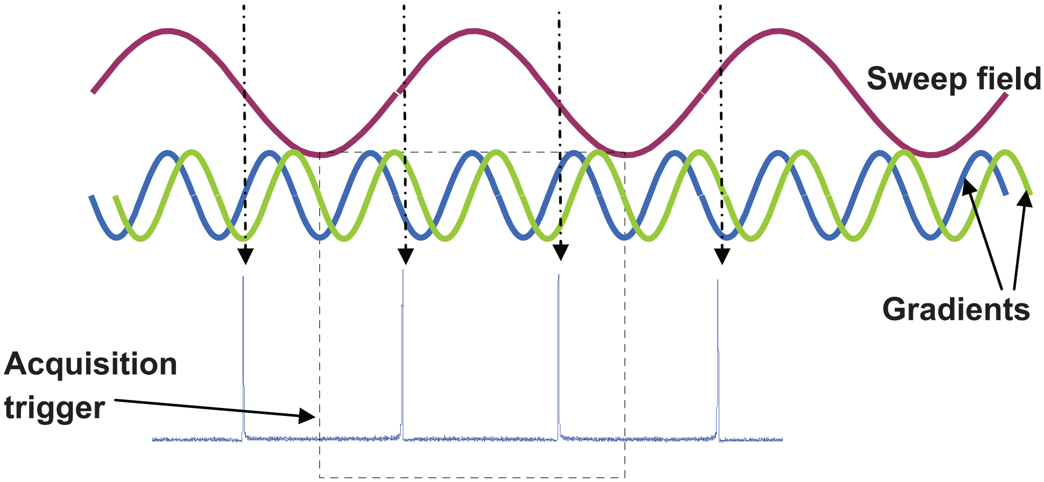

Figure 7. Direct detected absorption EPR signals of a phantom sample in the absence of gradients. The top sinusoid represents the rapid scan sweep (1.2 kHz), and the two high frequency sinusoids (blue and red, 4.8 kHz) represent the x and z gradients, which together provide the rotating gradient in the xz plane. The left side of the dotted rectangle represents the start of the trigger. 64 samples at 600 kS/s were collected for each gradient phase setting, giving rise to one downfield scan and one up field scan. Acquisition time per projection is 208 μs.

the matrix to generate the conventional 'rectilinear' sinogram followed by filtered back-projection to yield the image as shown in Figure 8. For 3D collection, all that is to be done is to apply the combination of the three sinusoidal gradients such that, vectorially, they will represent series (usually 64) 2D experiments with the 2D rotating gradient planes progressively tilted about the polar axis in steps of 2π/64 over a total span of 0–2π radians. The resulting data is sequentially shuffled and back-projected in two steps to generate the 3D image. With the current frequencies of the sweep and gradients we are able to generate data almost as fast as in time-domain EPR! (see Table 1).

Excellent 2D and 3D images of phantoms and *in vivo* mice tumor images have been obtained by this method, at speeds that can compare well with time-domain EPR imaging. We are in the process of adding hardware and appending the software for changing the frequency of the field sweep and gradient rotations, and to incorporate the capability of automating the collection of multiple gradient 2D and 3D images to generate respectively 3D and 4D spectral spatial imaging *in vivo*.

Time-domain EPR Imaging

Time domain EPR instrumentation

In the time-domain mode, one deposits a pulse on the spin ensemble placed in a suitable resonator by gating a continuous wave source of the electromagnetic radiation. Since NMR spectra are spread over a narrow of frequency range (10 to 100 kHz), the pulse width of RF is typically in the microsecond range. The time-domain response (the so-called free induction decay, FID) of the nuclei, which is in the millisecond—second range can be recovered after a typical spectrometer recovery time (dead time) of several microseconds. In time-domain EPR the time resolution in the experiment needs to be in the nanosecond range. EPR spectra cover a broad range of frequencies (several MHz) and therefore excitation pulse widths should be less than 100 ns, requiring the ability to deposit narrow intense pulses to disturb the spin system. After the pulsed excitation, the weak time-domain responses (which last only for time periods comparable to the spectrometer recovery time itself) have to be acquired with a fast digitizer at rates dictated by the frequency bandwidth of the resulting spectrum. The actual power of the pulse (pulse height) that is needed will depend upon the volume of the resonator and the conversion efficiency of the resonator in terms of the ratio of RF magnetic field to square root of RF power. The pulse width and power that will be used for *in vivo* imaging also has to take into

Table 1. CW Rapidscan-Rotating gradient direct detection measurement times.

1D Single 64 point projection	208 μs
2D image 64 × 64 points	52.4 ms
3D image 64 × 64 × 64 points	3.35 s

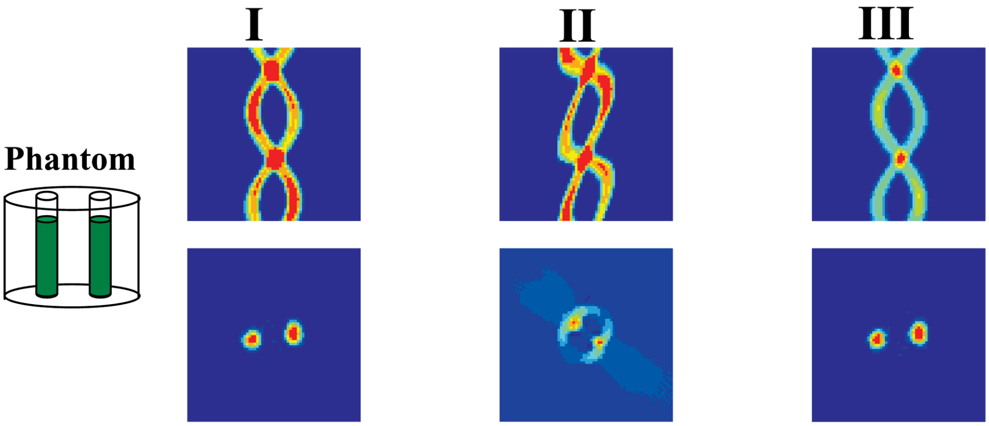

Figure 8. Conventional sinogram from a 2-tube phantom (on the left) and the corresponding filtered back-projected image (left column I) Skewed pseudo sonogram and the corresponding pseudo image obtained from the raw data when projections were collected with simultaneous sweep and rotating gradients (middle column II). Reshuffling the matrix leads to the correct sinogram and the expected image (last column III).

account one very important factor, namely, the specific absorption rate (SAR) (the time derivative of the incremental energy absorbed by, or dissipated in an incremental mass contained in a volume element) which, by convention, is the average energy in Watts dissipated per kg of body weight by the electromagnetic radiation during the imaging process. Several countries have come up with SAR standards. The Food and Drug Administration (FDA) of United States has recommended that the maximum energy that is deposited during MRI and other tissue radiation exposure protocols should not exceed a prescribed limit. The FDA SAR guidelines limit the energy dissipation to 0.4 W/kg whole body average, 8 W/kg peak at any 1 gm of tissue and 3.2 W/kg in the head. In Canada the SAR level is 2 W/kg whole body average.

In our imaging spectrometer, the RF signal and the local oscillator frequencies are generated from a phase-locked RF source at 800 MHz. From this, using frequency dividers, double-balanced mixers and band pass filters, frequencies of 500, 300, 320, 50, 20 and 10 MHz are derived. The use of a single master oscillator insures that the different frequencies derived will have a constant relative phase relationship with on another. The 300 MHz frequency is pulse-modulated using high-speed RF gates, which consist of GaAs SPDT switches. The pulses formed by these gates have rise/fall times less than 4 ns. The phase of the pulses was alternated between 0º and 180º during the data acquisition. The pulses thus formed were amplified using a 200 W Class A power amplifier (Model 5066RE, Ophir RF, Los Angeles, CA) and fed to the resonator through a diplexer. Pulses with widths in the range 50 to 100 ns were amplified up to a maximum of 280 Vpp. The transmitter and the receiver are to be isolated because the transmit power may be several hundred watts, while the induction signals from the spins may just be a few tens of nanowatts. We amplify the free induction signals by at least 65 dB before digitizing the same. Because of this, when the receiver gate is opened there should be minimal leakage from the transmit power which takes a characteristic time after the transmitter pulse is switched off to decay to the thermal noise level of the circuit. The isolation between the transmit arm and receive arm can be achieved by a transmit-receive switch such as a diplexer or a circulator. One can employ the so-called crossed-loop resonator (Quine, Rinard, Eaton et al. 2002) in which the resonator consists of a transmit coil and a receiver coil with their RF field axes mutually orthogonal which helps in isolating the transmitter and receiver and greatly reduces power leakage on to the detection arm. The diplexer provides the isolation by a set of crossed diodes which make the receiver arm non-conducting during the transmit cycle and prevents any reflections returning back to the transmitter arm during the receive cycle and is the standard method adopted in pulsed NMR. In our system we employ a standard $\lambda/4$ configuration diplexer (Murugesan, Afeworki, Cook et al. 1998). The diplexer has a standard pin-diode switch assembly in the transmit path and a shunt pin-diode switch in the receive path. These diodes were maintained in a back-to-back configuration to minimize the transients in the RF paths. This arrangement provided switching times on the order of 5 ns. The receiver isolation during transmit mode was 25 dB with a transmit insertion loss of 2 dB. The insertion loss during receive mode was 0.5 dB.

There is not much difference between the magnet/gradient coil requirements between CW and time-domain EPRI. In our system the main magnetic field was generated by a Helmholz pair (30 cm i.d.) of water-cooled coils (GMW, Model 5451, Redwood city, CA), with field homogeneity better than 200 ppm in an active volume of $5 \times 5 \times 5$ cm^3. A shielded 3-axes gradient coil system (BFG-350/10, Resonance Research Inc. Billerica, MA) with a digital power supply of 14-bit resolution (Danfysik DF7000, Jyllinge, Denmark) was used for imaging experiments. The gradient power supply (Kepco BPO 2020, Flushing, NY) was controlled through an IEEE interface and the gradient settling time was less than 100 µs. The maximum gradient that we could apply was around 50 mT/m along any axis, and this is more than adequate for time-domain data acquisition on small animals, such as mice.

A full description of the parallel resonator we routinely use has already been published (Devasahayam, Subramanian, Murugesan et al. 2000). Essentially our parallel loop cylindrical resonators are 25 mm diameter × 25 or 50 mm long, capable of accommodating a laboratory mouse. They had a Q of ~15 (achieved by a combination of over coupling and resistive damping) when loaded with the animal. In the smaller resonator, used for investigating tumors implanted on mouse legs, the 90° pulse length was 70 ns, and the dead-time was around 250 ns.

Our spectrometer can be operated either in a single channel mode at an intermediate detection frequency (IF mode) by mixing the induction signals at the carrier frequency (300 MHz) with a local oscillator frequency of 320 MHz, or in the quadrature mode with dual channel detection. In the quadrature mode, the signals were mixed with the carrier frequency down to base band using a quadrature mixer and digitized in two channels for the real and imaginary parts of the FID. In this mode, the RF power is effectively utilized and the phase and sign information of the signals is retained. All current measurements are carried out in the quadrature mode.

The signals received when the spectrometer recovers after the transmit pulse are weak and last only for a few μs. This signal needs to be amplified to a suitable level prior to digitization. Therefore the receive chain should have fast recovery and high gain. The first stage amplifier is critical. After suitable amplification, the resonance signals are isolated by appropriate band pass filters and delivered to the digitization module. Thus the choice of the front-end preamplifier is very important. In our current version we use a low noise (<1 dB), fast recovery (50 ns, as tested by us) preamplifier (Hi Level PHEMT Preamplifiers, Angle Linear, Lomita, CA). After the first stage amplification, the signal is filtered with a 300 MHz center frequency band pass filter having a bandwidth of 42 MHz (TTE/07766-KC6-300M-14P-50-6140, TTE Inc., Los Angeles, CA) and subsequently amplified by a low-noise amplifier (Miteq 2A 150, 25 dB, Hauppauge, NY) and an RF amplifier (gain 25 dB, Model MHW590, Motorola). Adjustable attenuators are used to set the appropriate levels. Our current version of the time-domain spectrometer uses an Acquiris data acquisition system (Model AP100, Acqiris USA, Monroe, CA 10950) with a maximum sampling speed of 500 Ms/s and with two channels and a PCI interface that has proved to be the best so far in terms of the flexibility of digitization rate, FID length and inter pulse delays. A schematic of the 300 MHz time-domain EPR imaging spectrometer currently in use in our laboratory has already been reported in detail (Murugesan, Afeworki, Cook et al. 1998).

Data acquisition and image reconstruction in time-domain EPRI

FID_FBP mode of EPR imaging: In our earlier time-domain image data acquisition and image processing in time-domain EPRI are quite similar to that described under CW EPRI. The projections are collected in the form of FIDs in presence of stationary gradients as free induction decay responses. These are subjected to a fast Fourier transform which gives us the projections that are, in principle, identical to those obtained in CW EPRI with a field sweep. These are then treated as mentioned before to produce images in 2 and 3 dimensions using filtered back-projection. The advantages and drawbacks of the time domain methods over the CW method have been reported (Yamada, Murugesan, Devasahayam et al. 2002). The filtered back projection method using the free induction decays (FID-FBP) is capable of fast RF EPR imaging of small animals such as mice. But imaging with larger gradients leads to prohibitively short T_2* compromising the image quality. The FBP-FID has inherent drawbacks such as image artifacts and line width limited resolution. Being a pure frequency encoding method, the FBP-FID requires accurate phasing of the sampled magnetization. Besides limiting the sensitivity of the spectrometer, the dead time also leads to considerable distortion in the spectral features. The missing time interval may be too large for proper image reconstruction at high offset frequencies when the dead time is comparable to T_2*. In addition, the T_2* of the FID depends on the spectral range according to the equation

$$1/T_2{}^* = 1/T_2 + \gamma_e \Delta B/2 \qquad [3]$$

where, T_2 is proportional to the natural line width and ΔB is the variation of magnetic field over the region of interest. This leads to a differential loss in the integrated intensity of the projections, causing artifacts in the back- projected image (Yamada, Murugesan, Devasahayam et al. 2002). Such artifacts will be significant for oblong objects under large gradients. Attempts to increase the resolution by increasing the magnitude of the gradients will lead to further reduction of T_2* according to Eqn. [3]. Besides, being a pure frequency encoding method, the inherent resolution is limited by the line width of the spin probe. Hence an alternative way of spatial encoding that would not be seriously affected by the relaxation time, capable of providing artifact free images, is crucial for the development of time-domain RF EPR *in vivo* imaging. Such a scheme, described below, is what we employ routinely in our imaging of mouse tumor models.

Single point imaging, SPI

The very short T_2^*s in the MRI of solids preclude the application of gradient pulses during the evolution of the spin system as in the regular imaging *in vivo*. Emid and Creyghton (Emid and Creyghton, 1985) proposed a novel pure phase encoding approach to overcome this and to achieve resolution enhancement in addition. This technique, known as single point imaging (SPI), (also known as constant time imaging: CTI), has been widely applied, in different modified forms, to solid-state NMR imaging (Gravina and Cory, 1994). The method essentially consists of generating k-space information in the presence of pure phase encoding static gradients and is shown to provide artifact-free images, because it does not measure the time evolution of the magnetization. The high-resolution capability of the SPI modality has also been recognized nearly 15 years ago in 1D EPR imaging (Maresch, Mehring and Emid, 1986). But, no further efforts have been made to evaluate the use of this technique in EPR imaging, perhaps due to the limitation posed by the long data acquisition time. A schematic representation of SPI technique is shown in Figure 9. A single, complex data point of the FID, at a fixed evolution time following the pulsed excitation, is collected in the presence of a static magnetic field gradient present from the start of the pulsed excitation till the data point is accumulated after a time duration denoted as ‘τ’. For one dimensional image data, the system is subjected to pulsed excitation and the signal (FID) amplitude is collected for each excitation at the same time interval ‘τ’. The gradient is incrementally ramped, in equal steps ΔG, from a value of $-G_{max}$ to $+G_{max}$. The amplitude variations of this single point correspond to phases accumulated as a function of the incremental phase encoding gradient for the duration ‘τ’. In other words, the spatial information is encoded in reciprocal space, $S(k)$, where $k = \gamma G\tau/2\pi$, by the amplitude cycling of the applied gradient G. Since the phase encoding gradients are ramped in steps from a positive to negative value through zero, the resulting amplitudes simulate a “pseudo echo” which upon FT provides the one-dimensional spin profile along the phase encoding direction. This is schematically shown at the right side of Figure 9. The SPI signal intensity, $S(\tau)$, is related to the local electron spin density, $\rho(\boldsymbol{r})$ along the gradient direction $\boldsymbol{r}$ by,

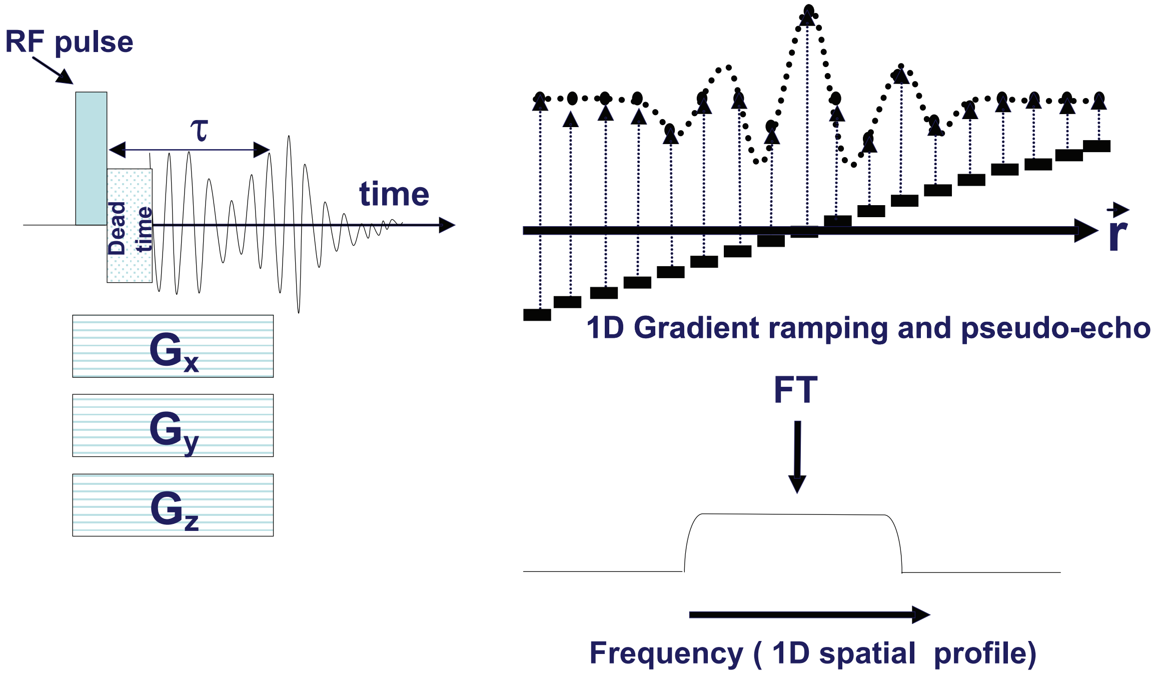

Figure 9. Schematics of Single Point Imaging (SPI). The FIDs are collected in presence of phase encoding gradients and the phase modulation on a given single time point after a delay τ leads to a response that is analogous to the gradient recalled echo in MRI. The gradients are ramped from positive maximum to negative maximum value in incremental steps, and the resulting phase modulation leads to amplitude modulation, encoding the spatial location of spins. Fourier transformation of the echo leads to the image. The gradients can be looped to generate 1, 2 or 3D k-space.

$$S(\tau) = \iiint_{allspace} \rho(r)\exp[i\gamma G.r\tau]dr \quad [4]$$

and in k-space formalism,

$$S(k) = \iiint_{allspace} \rho(r)\exp[i\gamma k.r\tau]dr \quad [5]$$

Thus the signal intensity, *S(k)* and the spin density, *ρ(r)* have a Fourier relationship and therefore direct Fourier image reconstruction algorithm can be applied. For 1D, 2D or 3D imaging, phase-encoding steps in one, two or three dimensions can be applied by a nested looping of the three orthogonal (x, y, z Cartesian axes) gradients. Since all the image information is acquired at *single time-point* after a *constant time interval* after the pulse, there is no information on spectral evolution. Hence the SPI images, in principle, are free from distortions due to the magnetic field inhomogeneity, susceptibility variations and g- and line width anisotropy. The point spread function (PSF) and hence the resolution is unaffected by T_2* because the magnetization is measured as a function of applied gradient and not as a function of time. The 1D resolution, Δz along the z-direction for a total one-dimensional field of view (FOV_z) is given by

$$\Delta Z = FOV_z/N = 2\pi/(\gamma_e G_z^{\max}\tau) \quad [6]$$

where N is the number of samples of k space measured in the *Z* direction and γ_e is the gyromagnetic ratio of the electron. The resolution, even for short T_2* species, is limited mainly by the maximum gradient strength and not by the line width of the EPR spin probe. Even for a broad resonance, image resolution independent of line width can be achieved. However, the field of view to be studied and the available B1 field will determine the G^{max}.

The field of view (*FOV*) in a given direction is given by

$$FOV = 2\pi/\gamma_e\tau\Delta G \quad [7]$$

where, ΔG is the incremental gradient step. As can be seen, the finer the gradient steps, or higher the values of τ, the *FOV* would be correspondingly smaller. However, for the entire field of view to be properly encoded, the pulse should have optimal power and width (τ_p) so that it can provide a uniform excitation spectrum for the entire frequency bandwidth $\Delta\nu$. In other words,

$$\Delta\nu \geq N/2\tau \text{ and } \tau_p \leq 2\tau/N \quad [8]$$

If these requirements are not satisfied, then, the high k-space data will be attenuated, resulting in the blurring of sharp edges in the spatial image. For maximum SNR, the time point, τ could be as close to the pulse as possible, immediately following the dead time. Although the pure phase encoding method produces high-resolution images with minimal artifacts, the SPI sequence can be time-inefficient because it requires N^2 excitations for a 2D image of N^2 pixels. For a τ of 800 ns, the optimum value of N = 21, for a 1 mm resolution when $\Delta G = 2$mT/m. Using 21 × 21 phase encoding steps, 2D SPI data image could be collected in 5 sec. with signal averaging 1000 responses per gradient settings, in our present data acquisition system. A 3D collection with 21 × 21 × 21 (9261) phase encoding steps with the same number of averages could be accomplished in about 2 min.

Spin-echo imaging

We mentioned earlier that EPR images can be constructed using the well-known filtered back-projection procedure after Fourier transforming the FIDs obtained in presence of gradients. The very short T_2* of most paramagnetic systems allow only part of the FIDs to be collected due to the recovery time of the spectrometer, and, in presence of large gradients, due to the interference of large bandwidth of frequencies the fraction of FID that can be gathered becomes shorter and shorter. The apparent transverse relaxation time T_2* is shortened in proportion to the magnitude of the frequency encoding gradient due to rapid dephasing. However, it is possible to employ the well-known Hahn echo sequence using a pair of 90-τ-180 pulses, and acquire the the echo after times on the order of the true spin-spin relaxation time of the spin probe. Such an echo based image quality is of course identical to that obtained from FID, except that one can now collect a series of T_2 (and not T_2*) weighted images. Further, the peak of the echo which corresponds to a coherent signal with all magnetization in-phase will help generate pure absorption line shape and will generate images which are bound to be more resolved than the ones generated from FIDs which are usually processed in the magnitude mode and hence inherently broader. A series of echoes acquired for different τ values and images reconstructed from them can provide spatially resolved

T_2 information just as in T_2-weighted MRI (Mailer, Subramanian, Pelizzari et al. 2006). It is to be noted that the 90° and 180° pulses should have width and amplitudes that will cover the entire bandwidth of the frequency spread of the system under the frequency encoding gradients. The very short transverse relaxation times of paramagnetic spin systems do not allow slice selection or pulsed gradients, familiar in MRI, to be employed in EPR imaging.

Oxymetric (T_2- and T_2*- weighted) EPR Imaging

The most important application of EPR imaging *in vivo* is its capability to report non-invasively, the *in vivo* tissue oxygen concentration (pO_2) quantitatively, based on spatially resolved spectral information of the spin probes. MRI uses T_1 and T_2 (in the presence or absence of contrast agents such as Gadolinium (III) chelates) to distinguish different types of tissue based on the local relaxation times. In BOLD-MRI (Ogawa, Tank, Menon et al. 1992) the differential oxygenation based on the ratio of oxy- to deoxyhemoglobin is used to produce the contrast. In EPR differences in the concentration of dissolved oxygen can act as a natural internal contrast agent and the *in vivo* line width or relaxation time of the spin probe can be used as *in vivo* oxygen reporter. The width of the EPR lines are affected by spin-spin broadening and should provide a direct measure of pO_2 in a non-invasive manner. In simple terms, we will expect anatomical regions containing the spin probe, which are hypoxic, to give narrow lines (longer T_2 or T_2*) whose time-domain response will last longer compared to signals arising out of regions which are normoxic (shorter T_2 or T_2*). This would be the time-domain analog of spectral-spatial imaging. Such a spectral-spatial imaging scheme can also be carried out using the SPI data. Since our fast digitizer acquires SPI data, we collect close to 1000 points of time responses at 200 Ms/s sampling rate, following the dead time. For the image reconstruction we need just a single point in this FID, and therefore each set of SPI data contains information for image reconstruction as a function of delay from the start of the collection. Several hundred images can be reconstructed from the set of FIDs. Although a particular constant time point does not have spectral information, a sequence of time points contain pixel-wise T_2* information. However, as the single point is removed farther and farther from the start, the *FOV* decreases producing a 'zoom-in' effect in the images, the latter time points affording a better resolution. For retrieving the transverse decay characteristics, it is essential that all images be interpolated to a common *FOV*, so that each corresponding pixel in every image will report on the same physical location in the object. This can be done either by zero-filling the phase-encoded k-space data in inverse proportion to the delay or by numerical interpolation. Once this is done, the decay of intensity in a given pixel will report on the T_2* of the spin in that location and hence report on the line width. Unlike the FID-FBP mode of collection, the image data at a given constant delay from the pulse does not have contribution from susceptibility and field inhomgeneity. In otherwords, the sum total modulation from the time-dependent Hamiltonians reamin constant at the single point, leaving only the net phase modulation due to the gardient and the spin distribution. However, images from a sequence of single points of the FID will be waited by the local T_2*. In order to have a reliable T_2* it is imperative that we keep the inherent resolution of the images as close as possible. Balcom et al. (Balcom, Beyea, Green et al. 1996a; Balcom, Beyea, Green et al. 1996b; Halse, Rioux, Romanzetti et al. 2004) have shown in the case of solid polymers, that one can use different gradients, namely, higher gradients for shorter delay and lower for longer delays. Since the *FOV* is inversely proportional to the product of the gradient step ΔG and the delay τ, this strategy keeps the resolution and SNR of the images in a close range and allows the derivation of spatially resolved T_2* which are reproducible, and hence can be used for quantitative characterization. (See Fig.10 and the caption for more details).

This mode of spectral-spatial image reconstruction technique denoted as time-domain constant time spectral-spatial imaging (FT CT-SSI) is analogous to the CW spectral-spatial imaging scheme in providing spatially resolved spectroscopic information such as line widths. One advantage of CT-SSI is its ability to avoid missing angle issues(Eaton et al. 1989) by simple interpolation, as against the iterative methods generally employed in the CW method. The same procedure can also be applied to CW imaging (Matsumoto, Chandrika, Lohman et al. 2003). The only difference is that projections are to be collected using a Cartesian raster with gradients applied exactly analogous to the time-domain SPI mode. Once the projections are obtained, what

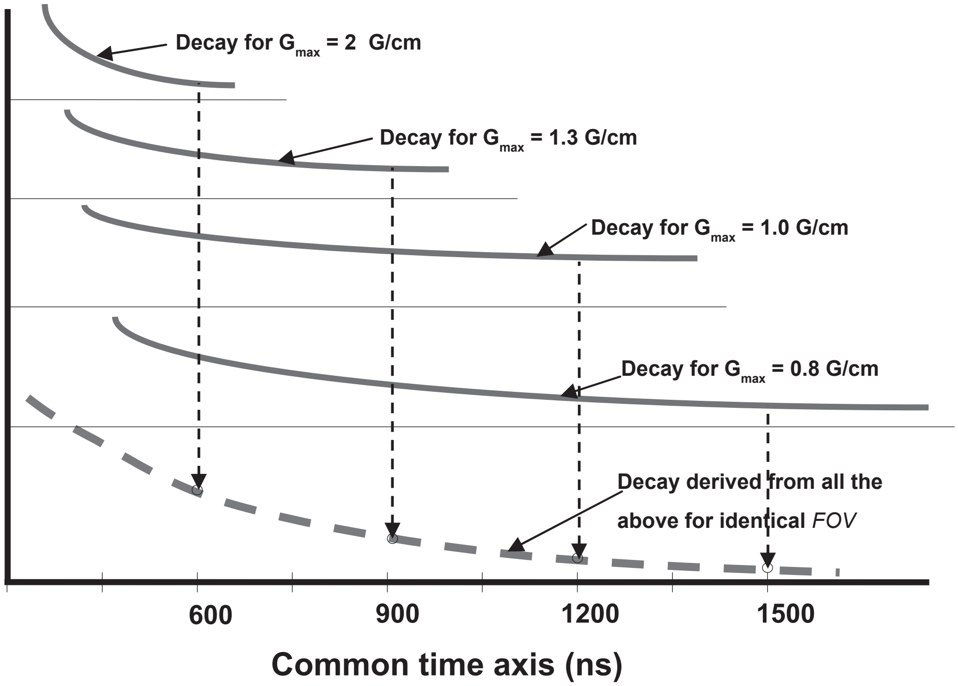

Figure 10. Schematics of the multigradient SPI experiment to evaluate T_2* decay. A series of interleaved SPI experiments at different gradients allows selecting single point images at different delays with almost identical resolution. At higher gradients the decay rate is faster and SNR is better at short delays, and at lower gradients the decay rate is slower and SNR is comparable at larger delays. Combining the results from multigradient experiements the decay rate when the *FOV's* are almost the same leads to reproducible single exponential T_2* and apparent line widths.

remains is to apply an inverse Fourier transform and then follow identical procedures to get the line width information. There is a subtle difference between the values of T_2* obtained from CW CT-SSI and time-domain CT-SSI. In CW, projections are obtained at constant frequency with field sweep, and there is no dead time or gradient induced broadening due to interference of isochromats brought about by the frequency spread by the gradients. Hence one gets in CW CT-SSI the true line widths (as would be obtained in the absence of gradients), whereas in time-domain CT-SSI one gets the local T_2*. In order to use the local T_2* as a quantitative oxygen reporter it is essential to calibrate the system with suitable fiducials under conditions of identical gradient magnitudes and gradient steps. Compared to the conventional CW spectral-spatial imaging with filtered back-projection, the CW CT-SSI and FT CT-SSI procedures are much faster.

Overhauser magnetic resonance imaging, OMRI

OMRI (also known as Proton Enhanced Double Resonance Imaging, PEDRI) is a double resonance technique in which a system containing protons and unpaired electrons is first subjected to a strong resonance irradiation at the electron frequency to saturate the spin system. This leads to a transfer of polarization to protons and other nuclei, which are dipolar coupled to the electrons producing a large population difference between the nuclear spin energy states. As long as the saturation is carried out for times on the order of T_1 of the protons, and the protons are immediately subjected to resonance detection, one gets an enormous increase in the signal due to the Overhauser effect, also known as Dynamic Nuclear Polarization. The spatial resolution of the image is not governed by the line width of the free electron probe, but the degree of saturation, which, however, depends on the line width. Overhauser-enhanced proton imaging has also been carried out with probes such as nitroxyl radicals, (Grucker, 2000) but the enhancement factors, although not very high, could provide functional information. A series of stable paramagnetic spin probes based on the TAM radicals were introduced by Nycomed Innovations, who also carried out functional OMRI measurements on small animals, to quantitatively evaluate tumor perfusion and tissue hypoxia (Golman, Leunbach, Ardenkjaer-Larsen et al. 1998;

Golman, Leunbach, Petersson et al. 2002). The instrumental requirements for OMRI, the basics of Overhauser enhancement and the way in which one can use OMRI data to quantify tissue oxygenation levels have been already reported (Golman, Petersson, Ardenkjaer-Larsen et al. 2000). In short, the net enhancement of proton intensity depends on the concentration of the paramagnetic contrast agent, the RF power and its duration used for saturating the EPR signal, and in the local line width of the spin probe which is subject to broadening by *in vivo* pO_2. It can be shown that by performing an interleaved OMRI imaging experiments using two different EPR power levels, with all other parameters identical, it is possible to quantitatively derive pixel-wise spin probe concentration and oxygen concentration. OMRI, thus, is an independent method to measure *in vivo* pO_2 in tumors, and has been applied to evaluating tumor hypoxia in small animals (*vide infra*). The OMRI pulse sequence is shown in Figure 11.

Summary of Various EPR Imaging and Oxymetry Results

All measurements were made using trityl based spin probes. Early measurements were based on the Fourier transformation of FID followed by filtered back projection and gave good results both on phantoms and small animals such as mice *in vivo* at low gradients (Subramanian, Yamada, Irie et al. 2002a). Semi-quantitative T_2* weighted *in vivo* oxymetry could be performed using the differential attenuation of spatially resolved intensities as a function of the progressively delayed processing of the FIDs. However, for large gradients and oblong objects, the images were fraught with artifacts due to a substantial loss of signal under the spectrometer recovery time, and soon this method was replaced by the more reliable single point imaging scheme involving pure phasing encoding scheme, as detailed below.

Results from single point imaging

Because of the pure phase encoding and the fact that other time dependent Hamiltonians do not have net effect on the modulation at the constant time point chosen for the entire image reconstruction, makes the resolution of the image in SPI independent on the line width, and under ideal condition, with only the point spread function of the instrument deciding the resolution. This is demonstrated by the excellent 3D image of a glass spiral of internal diameter of the tube being 1.4 mm filled with 2 mM Oxo-63 using 3D phase encoding, shown in Figure 12. It was not possible to produce such a clearly resolved image using the FID-FBP method. Even a 90-τ-180 spin-echo followed by back-projection did not produce such a good image at identical gradient strength.

Single point oximetric imaging

For quantitative oxymtric imaging, we adopt the multiple gradient T_2* weighted imaging procedure proposed by Balcom et al. In this method single point images are generated for three different maximum gradients in an interleaved fashion. From the results of three experiments, a total of 12 SPI images were constructed. Since gradients and the delay are different they all will have different

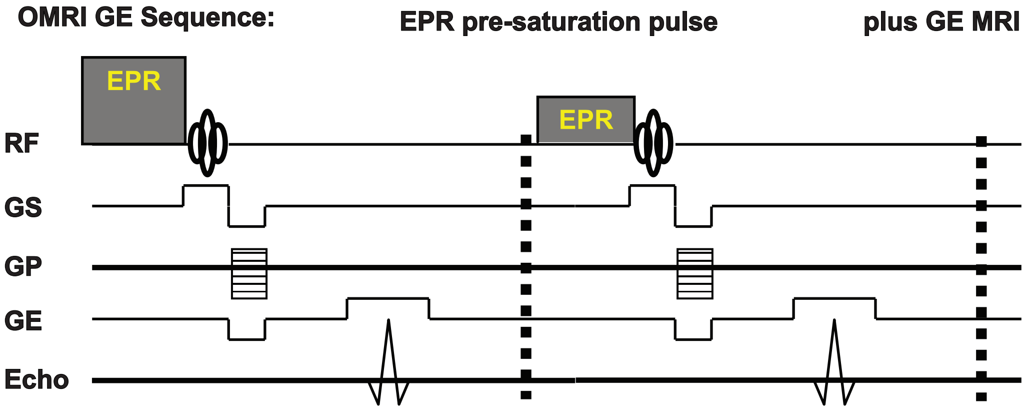

Figure 11. Schematics of the OMRI pulse sequence which is quite similar to the MRI gradient recalled echo sequence except for the electron pre-saturation pulse indicated by EPR. Two gradient echo images are sequentially measured for two different power levels in order to evaluate the two unknowns, the probe concentration and the *in vivo* pO_2. What is not shown is that EPR irradiation is carried out at 226 MHz at 8.1 mT and just before MRI at 640 kHz, the field is ramped up to 15 mT.

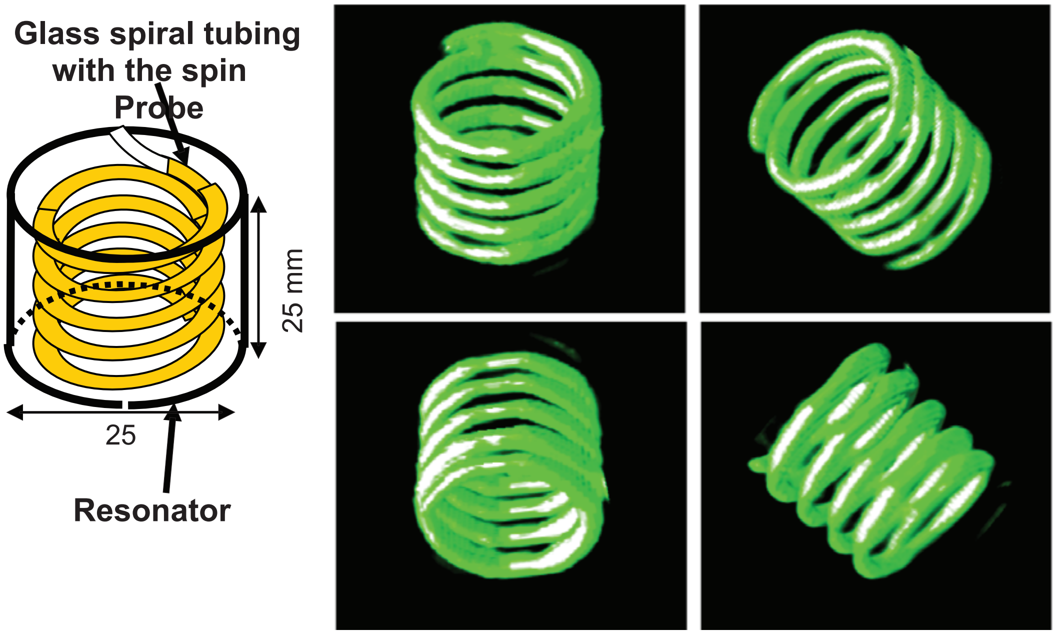

Figure 12. 3D SPI image of a Spiral phantom. Schematics of the glass spiral tubing filled with 2 mM Oxo63 in saline is shown on the left. The inside diameter of the glass tube was 1.4 mm and the capacity of the spiral was around 450 μL. The gradient increment was 0.3 Gauss/cm and the maximum gradient was 1.5 Gauss/cm. The data matrix size was 11 × 11 × 11 (1331 single points) and the size of the image matrix was 64 × 64 × 64. The 3D rendering at a few orientations shown on the left was carried out using the software Voxelview® in a silicon graphics Indigo2 workstation. The quality of the image is very good and dimensions matched well with those of the phantom.

FOVs. By zero-filling the k-space data in inverse proportion to the delay from the excitation pulse, it is possible to generate images of identical *FOV*, sequentially weighted voxel-wise by the local T_2*. By using phantoms of known pO_2 it was possible to have calibration of apparent line width $(\pi T_2^*)^{-1}$ versus oxygen partial pressure to arrive at spatially resolved oxygen maps. The linearity of the apparent line width based on T_2* is evident from the results on a 4-tube oxygen phantom shown in Figure 13. Resonator size, filling factor and the gradient magnitudes being kept unaltered, the pO_2 dependent line widths are reproducible and can be used for quantitative evaluation of *in vivo* oxygen distribution. Results from the imaging and oxymetry of SCC tumor measured using a 3-gradient 3D SPI are summarized in Figures 14, 15 and 16, where the captions detail the measurement and results. It was possible to assess the oxygen distribution quantitatively in several tumor types, identify hypoxic cores, and also monitor the changes in oxygenation when the animals were allowed to breathe oxygen rich gases such as Carbogen.

Overhauser Imaging of tumor hypoxia

OMRI measurements have also been carried out using TAM probes as well as nitroxyl spin probes. The reliability of the OMRI method to quantify spin probe concentration and oxygen concentration was found to be quite good from experiments carried out on calibrated phantoms and on whole body images of rat. With the animals breathing air with different percentages of oxygen, it was possible to evaluate the differences in the blood oxygenation levels quantitatively. We have used the OMRI method to investigate oxygen distribution and changes in oxygenation levels in tumors in a mouse model (Krishna, English, Yamada et al. 2002). Female C3H mice bearing an SCC (squamous cell carcinoma) tumor (approx. 1 cm in dia.) in one of the hind legs were imaged after intravenous infusion (via. tail-vein cannulation) of 150 μL of 100 mM Oxo63. Mice were anesthetized for imaging experiments by allowing them to breathe gas mixtures containing 1.5% isoflurane and air or carbogen (95% O_2, 5% CO_2). OMRI images were obtained without any electron irradiation and subsequently with two interleaved power levels (45 and 3 W) of electron irradiation. Before Oxo63 infusion, a bolus of gadolinium diethylenetriaminopentaacetic acid (GD-DTPA) was introduced in the bladder (urinary tract catheterization) to minimize the strong image intensity from the bladder. An appropriate slice was selected after the spin probe administration. 2D coronal

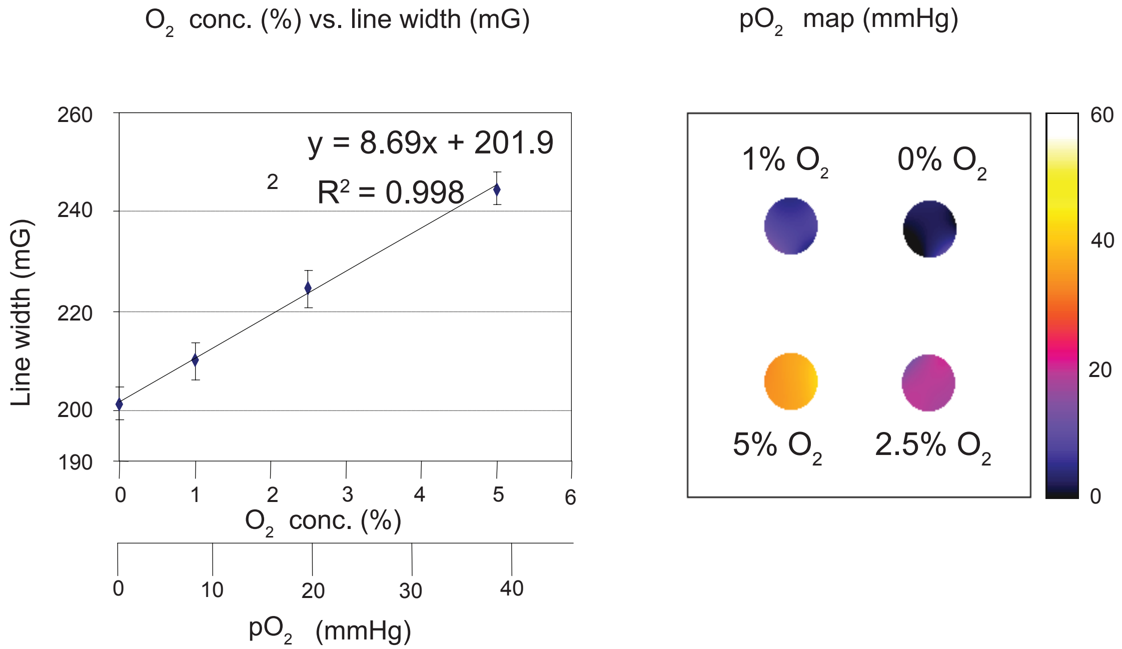

Figure 13. *Left*: The linearity of the T_2* based line width versus the dissolved oxygen concentartion for a 4-tube phantom with 2 mM Oxo63 saturated respectively with 0, 1, 2.5 and 5% oxygen, obtained from a 3-gradient, 21 × 21 × 21 steps oxymetric SPI 3D imaging data. *Right*: The corresponding color-coded oxygen images clearly distinguishing small differences in oxygen concentration.

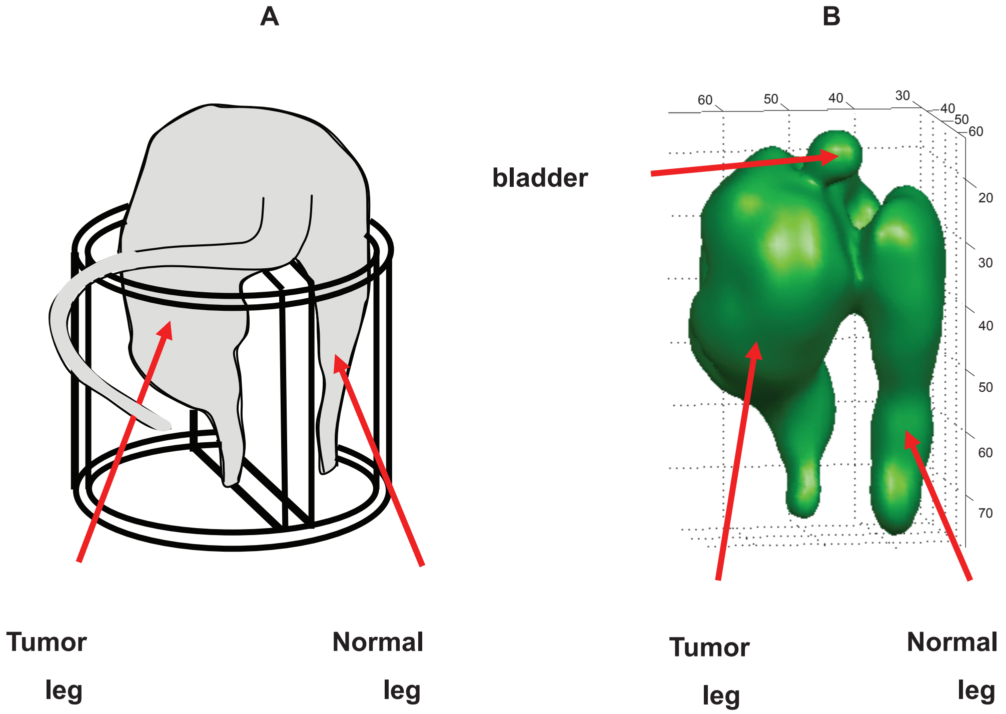

Figure 14. *Left*: The cartoon of a C3H mouse with its tumor-bearing and normal legs placed inside a 25 × 25 mm cylindrical resonator, separated by a Lucite partition. *Right:* After the mouse was infused with 75 µL 100 mM Oxo63 (approx. ~3 mM probe concentration in the blood), 3D SPI images were obtained using a maximum gradient of 1.2 G/cm, 21 × 21 × 21 gradient steps and 2000 averages in about 2.5 min. Surface rendered 3D image showing clearly the excellent image of the uniform outer distribution of the spin, the location of the tumor and the bladder.

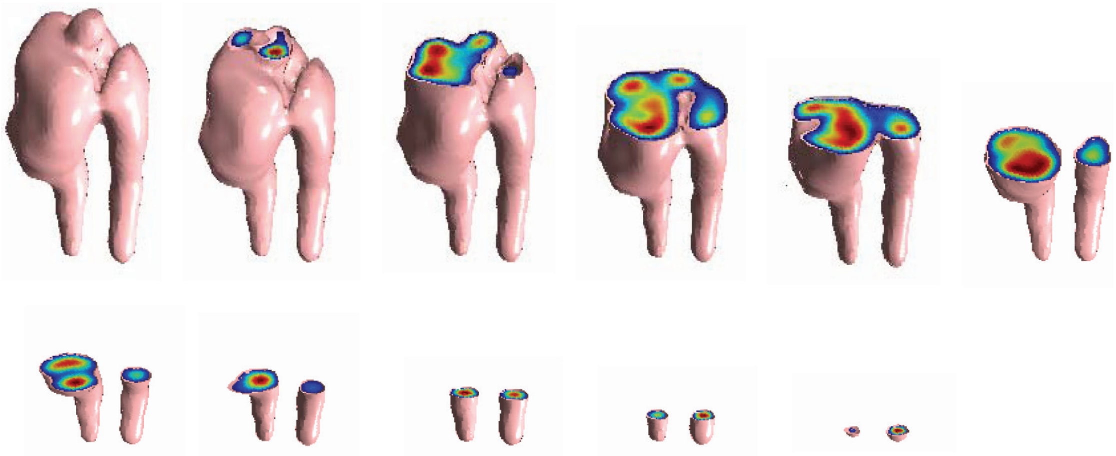

Figure 15. Axial cut-away views of spin distribution in normal and SCC tumor-bearing legs of a C3H mouse from 3D single point EPR image data shown above. 2D slices shown at 2.5 mm intervals. It can be clearly seen the tumor is preferentially perfused with blood compared to normal leg.

images of slice thickness 5 mm passing through the tumor and containing the kidneyswere acquired. OMRI mages were also acquired after allowing the mouse to carbogen for 15 min. Approximately the same experimental conditions used for OMRI were used for pO_2 measurements by the Eppendorf electrode. Two tracks parallel and two tracks perpendicular to the femur (total of 55 individual readings) were used to determine the median oxygen tension in each tumor. OMRI results and the distribution of spin concentration and pO_2 based on the calculations reported previously (Krishna, English, Yamada et al. 2002) and are summarized in Figure 17. It was found that the

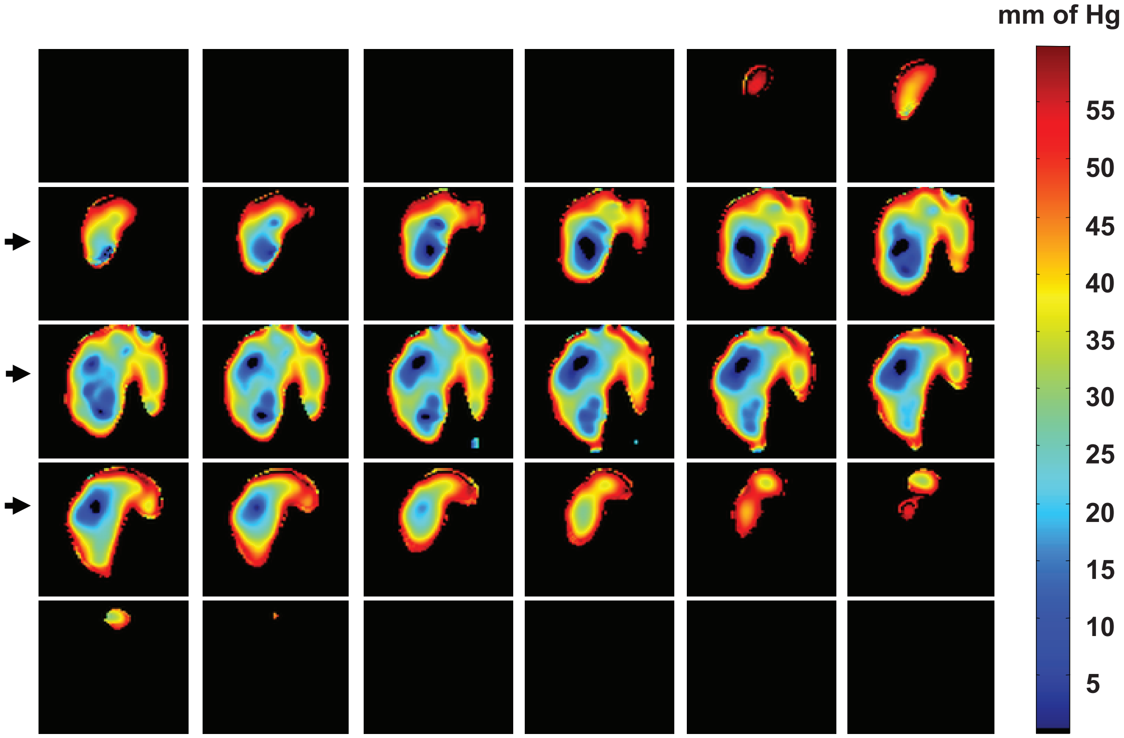

Figure 16. Coronal slices (1.1 mm thick) of oxygen distribution through the normal and SCC tumor-bearing legs of a C3H mouse derived from a 3-gradient 3D SPI image data based on T_2*. The total measuring time was 7.5 min. The hypoxic zones with near-zero pO_2 on the tumor leg, and the relatively uniformly oxygenated normal leg can be clearly monitored. The heterogeneity of oxygen distribution in the tumor leg is also clearly seen.

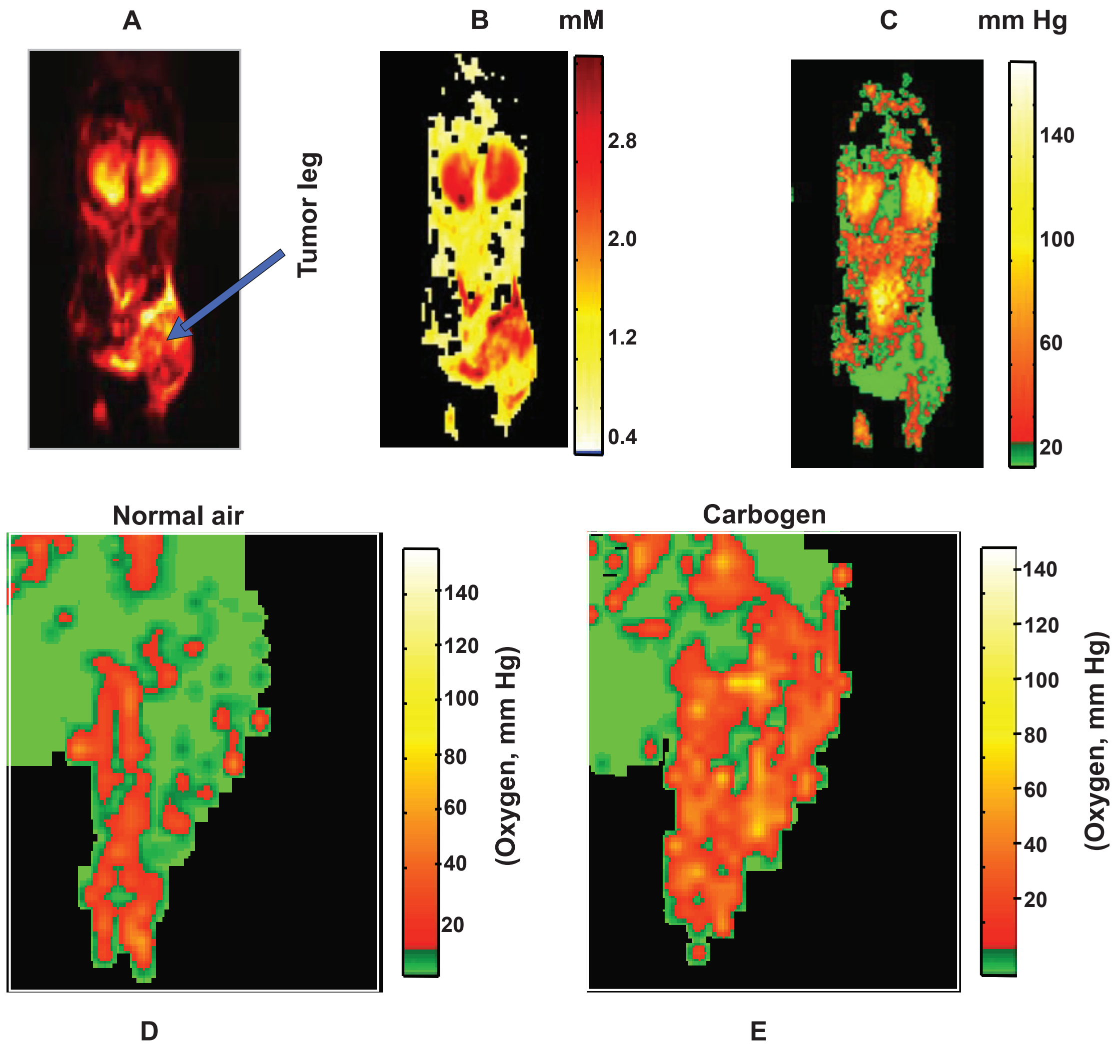

Figure 17. A. Coronal image (5 mm slice) of a C3H mouse with SCC tumor implanted in one of the legs taken at 640 kHz (low field MRI) with Overhauser enhancement. The kidneys and the tumor areas are well perfused by the spin probe and show good enhancement. **B.** Calculated spin probe image showing up to 3 mM concentration of trityl in the tumor. **C.** Calculated oxygen image showing close to 80 mm of pO_2 in the kidneys and very low ($<$10 mm) pO_2 in the tumor zone. **D.** Zoomed-in image of the tumor-bearing leg showing large areas of near-zero (hypoxic) pO_2. **E**. Oxygen map of the same slice as **D,** but the when the mouse is allowed to breathe Crabogen (95% O_2/5% CO_2) clearly showing increased oxygenation.

kidneys showed a fairly uniform distribution of spins, while the tumor zone was quite heterogeneous. Oxygen maps also showed a hypoxic core in the middle of the tumor for air-breathing mice (median pO_2: 5 ± 1.44 mmHg; $n = 5$), which upon Carbogen breathing got increased (median pO_2: 18.8 ± 1.3 mmHg; $n = 5$). Comparison of pO_2 histograms from the tumor region from OMRI and Eppendorf electrode measurements showed almost similar results (Eppendorf: air-breathing, median pO_2: 1.4 ± 0.1 mmHg; $n = 14$, and carbogen breathing: median pO_2: 15.8 ± 1.8 mmHg; $n = 7$). This shows that fairly reliable and repeated oxymetric measurements can be done in small animals with the OMRI modality. Identical results were obtained by evaluating the changes in C3H mouse SCC tumor oxygen distribution using single point multi-gradient oxymetric EPR imaging. The main distinction between OMRI and EPRI is that the OMRI needs at least 5 to 10 times more in the spin concentration to provide enhancements that can provide quantitative oxymetry, and the oxygen resolution is also somewhat less than that using direct EPR imaging.

Recent results from EPRI-MRI Co-registration

EPRI can provide a 3D distribution of externally introduced spin probe and can additionally provide the *in vivo* distribution of oxygen, and if the paramagnetic spin probe is redox sensitive it can also provide valuable information on *in vivo* tissue redox status. However, since the spin probes do not perfuse freely into the entire anatomy of the subject, detailed anatomical images cannot be expected from EPR image alone. However, since *in vivo* MRI deals with the distribution of water at levels of several tens of molar concentration, it provides detailed 3D anatomical images at high resolution, and can also provide, via volume selective spectroscopy detailed information on the distribution and changes of several metabolic intermediates. Many of the *in vivo* biochemistry (some aerobic and others anaerobic) may also be depend very much on *in vivo* pO_2 and tissue redox status. Likewise, X-ray CT, positron emission tomography and other fluorescence-based imaging are capable of providing complimentary diagnostic imaging. It is therefore natural that multimodality imaging, that may provide correlated and enhanced *in vivo* information, is becoming attempted by many research groups (He, Deng, Li et al. 2002; Matsumoto, Nagai, Yamada et al. 2005). Many functional imaging modalities such as BOLD, functional imaging of the brain, MR angiography, blood volume, and apparent diffusion constants are fairly routine in modern clinical MRI. Since the only difference between proton and electron magnetic resonance is the ~660 fold increase in the magnetic field strength in the case of the latter, for a given frequency of measurement, it is straight forward to perform EPRI and MRI in the same resonator assembly without moving the animal. The choice of 300 MHz for EPRI makes it convenient for measurements in the standard small animal 7T imager available to us operating at the same frequency. The only additional adjustment we make is to make these resonators switch between a low Q (~15) for EPR and increase to a high Q (~300) for MRI. We have fabricated a gantry consisting of an EPR resonator holder that slides into our 10.5 mT magnet, which can be transferred immediately after EPR to a larger holder and fastened without disturbing the anaesthetized animal and placed in the 7T MRI magnet for performing MR functional images. Sequential scans with the two modalities employing a common resonator enable pO_2 maps with anatomic guidance. Also, additional information gathered from MRI such as blood flow, blood volume, and water apparent diffusion coefficients (ADCs) aids in a more complete understanding of tumor physiology. Our pulsed EPR imager enables oxygen imaging of a preclinical animal model and can acquire pO_2 maps in almost real time for 2D and in minutes for 3D. Further, it was possible for the first time, to choose regions of interest (ROIs) based on pO_2 status and examine, using magnetic resonance spectroscopy (MRS), the levels of metabolites such as lactate, choline, etc., which may reflect the glycolytic states in the same regions. The results from this study show that (a) it is possible using EPR and air/carbogen cycling in the inspired gas to obtain spatial information pertaining to perfusion-limited hypoxia in tumors in a living animal. (b) The relationship between blood volume, blood flow, and pO_2 status from the tumors can be examined; there appear to be situations where substantial hypoxia may exist even in regions exhibiting blood flow. (c) High levels of lactate indicative of glycolysis, even in normoxic regions of tumors, were identified using sequential EPRI and MRS. This is a first report to our knowledge to simultaneously provide pO_2 levels and lactate levels in specific regions of tumor, visualizing the predominance of aerobic glycolysis in normoxic regions of tumors in intact animals (Gatenby and Gillies, 2004). The EPRI/MRI co-registration results are summarized in Figures 18–20 and the detailed description of this work was published recently (Matsumoto, Hyodo, Subramanian et al. 2008).

Summary and Future Directions

We have seen that time-domain and CW *in vivo* EPR imaging using non-toxic, implantable or water-soluble, biocompatible spin probes, trityl based free radicals, lithium phthalocyanine derivatives and nitroxides provide very valuable *in vivo* physiological information. As to what mode of approach, whether time-domain or CW, should be chosen will depend on the nature of the particular spin probe used and the kind of physiology investigated. When temporal resolution (because of fast pharmacokinetics) is of importance, time-domain methods would be the preferred choice. Added advantages of time-domain methods over CW methods are the availability of spectral information co-registered in time-domain data of the spatial image itself. The SPI mode of spatial encoding promises superior quality of image data. With improved data collection strategies, SPI may in fact

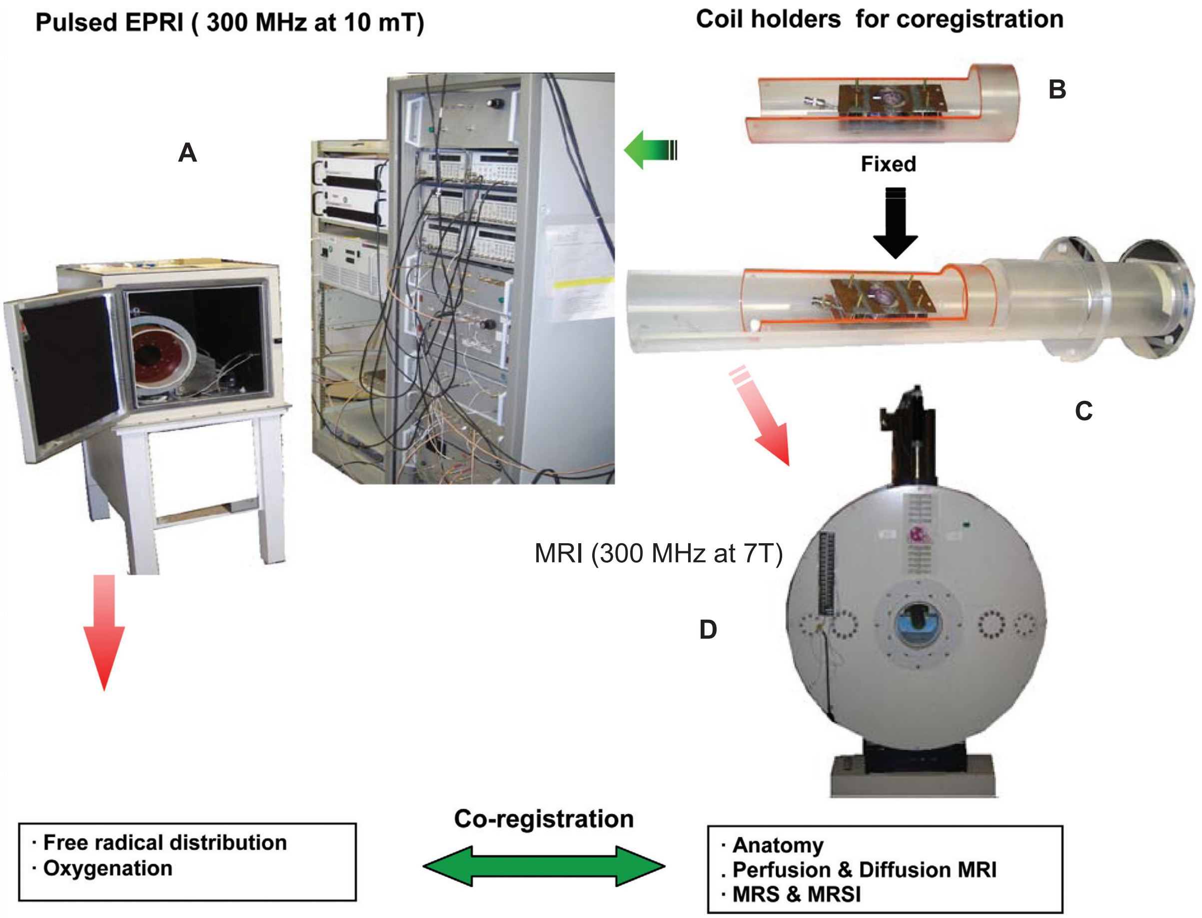

Figure 18. Schemaitic representation of EPRI-MRI coregistration experiment. **A.** The 300 MHz EPRI hardware. **B**. The resonator holder assembly that fits into the EPR magnet during EPR imaging. **C.** The MRI gantry that co-axially holds the EPR-resonator assembly and fits in the 7T MRI magnet for performing various functional MR imaging. Immediately following EPRI the mouse along with EPR resonator is fixed on to the MRI gantry without the need to move the mouse. A switch in the resonator circuit allows going from low Q (15 for EPRI) to high Q (200 for MRI) **D.** The 7T MR spectrometer (Bruker Biospin).

turn out to be the method of choice for small animal imaging in time-domain EPR. The conventional (90°-τ-180°) spin-echo Fourier transform followed by filtered back-projection also leads to T_2 weighted images with the contrast capable of providing quantitative oxymetry. However, images obtained from projections derived by the FT of echoes are not as well resolved as those from SPI modality presumably due to the fact that the echoes gathered in the presence of the gradients are subject to T_2*relaxation (only the peak of the echo decays with the time constant T_2), as well as susceptibility artifacts, although these somewhat less resolved images are weighted by T_2 as a function of echo-delay τ and give quantitative estimate of in vivo pO_2. The very short T_1 and T_2 of electron spin systems allow rapid data collection via pulsed methods leading to high temporal resolution and reliable pharmacokinetics.

However, recent developments in the CW arena such as spatial encoding with fast rotating gradients, the implementation of rapid scan involving direct detection, and imaging in presence of sinusoidal rapid scan and rotating gradients and direct detection make the CW approach equally competitive. The CW method has the additional advantage that it does not require spin probes with very narrow line width.

Before practical human applications can be envisaged, there are several aspects of both time-domain and CW *in vivo* EPRI that still need to be addressed. Foremost among these is the availability of FDA approval for the narrow-line spin probes. Although the TAM derivatives are very promising with respect to bicompatibility, FDA approval is still awaited. Future directions should also address the synthesis of other suitable oxygen-sensitive

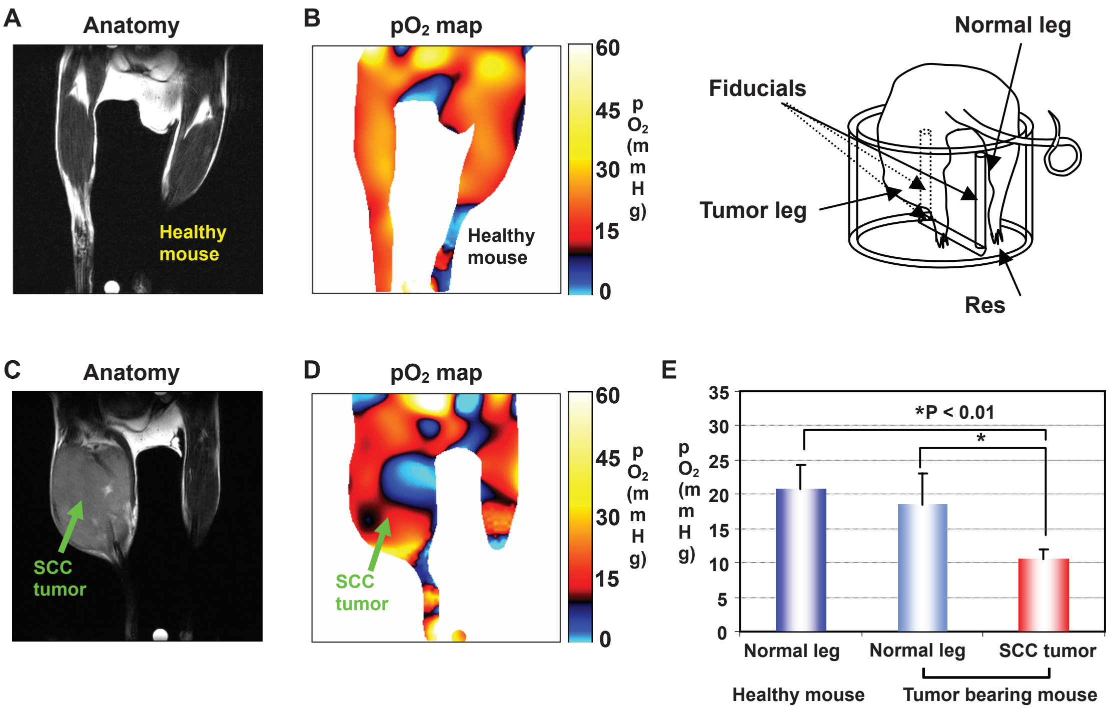

Figure 19. EPR oxygen imaging of normal muscle in live mice. EPRI method allows the pO_2 map from deep in tissue of healthy mouse to be obtained. The anatomic image from MRI (**A**) of the lower body of a healthy mouse (without tumor bearing) and corresponding pO_2 map from EPRI (**B**) showed that the normal muscle region had relatively homogeneous pO_2 distribution. The anatomic image (**C**) and pO_2 image (**D**) were also obtained from the contra-lateral normal leg of a SCC tumor-bearing mouse, and compared with that of a healthy mouse. (**E**) There was no significant difference in pO_2 between normal muscle tissues with or without tumor bearing as opposed to the significant, lower pO_2 in tumor region of the SCC mouse.

narrow-line paramagnetic compounds for use in both CW and time-domain *in vivo* spectroscopy and imaging. In the pulsed mode of EPR, we have to quantitatively evaluate the SAR problem since it involves the application of intense RF pulses of very short duration to larger biological objects. In case the SAR exceeds FDA set limits, perhaps one has to resort to array coils with multi-channel transmit-receive arrangement for reduced overall SAR. Stochastic or pseudo random pulsed excitation coupled with correlation techniques (such as Hadamard transform) have been developed for solid state deuteron NMR which employ RF powers reduced by at least two orders of magnitude, and yet achieve bandwidths and SNR comparable to the high power single pulse mode of excitation (Ernst, 1970; Ziessow and Bluemich, 1974). We have already carried out EPR experiments at 300 MHz on phantom objects with pseudo random excitation and Hadamard transform, and are able to reduce the power requirements by at least an order of magnitude without compromising the sensitivity (Pursley, Kakareka, Salem et al. 2003). The use of the latest DSP (digital signal processing) techniques that have made a revolution in the cellular communication area, in improving EPR spectrometer sensitivity, will be of considerable importance and are being implemented in our spectrometer (Pursley, Salem, Devasahayam et al. 2006). Sub-sampling techniques, that apparently defy the Nyquist theorem, are also being implemented in time-domain as well as CW techniques to take advantage of better bit-resolution achievable in low frequency digitizers (Hyde, Mchaourab, Camenisch et al. 1998; Pursley, Salem, Pohida et al. 2005). Development of high sensitivity resonators, especially for time-domain EPR for large volume applications is another important area. Pulse shaping (Freeman, 1998) which is a standard technique in accomplishing uniform selective excitation in NMR and slice selection in MRI has not yet been explored in time-domain EPR until recently. The main bottleneck had been the non-availability of sub-nanosecond time-resolution required for constructing decent, tailored pulse shapes such as multilobe sinc or Gaussian with total widths under 100 ns. These have now become available, and our laboratory has already implemented the use of shaped pulses in our 300 MHz time-domain EPR (Devasahayam, Murugesan, Matsumoto et al.

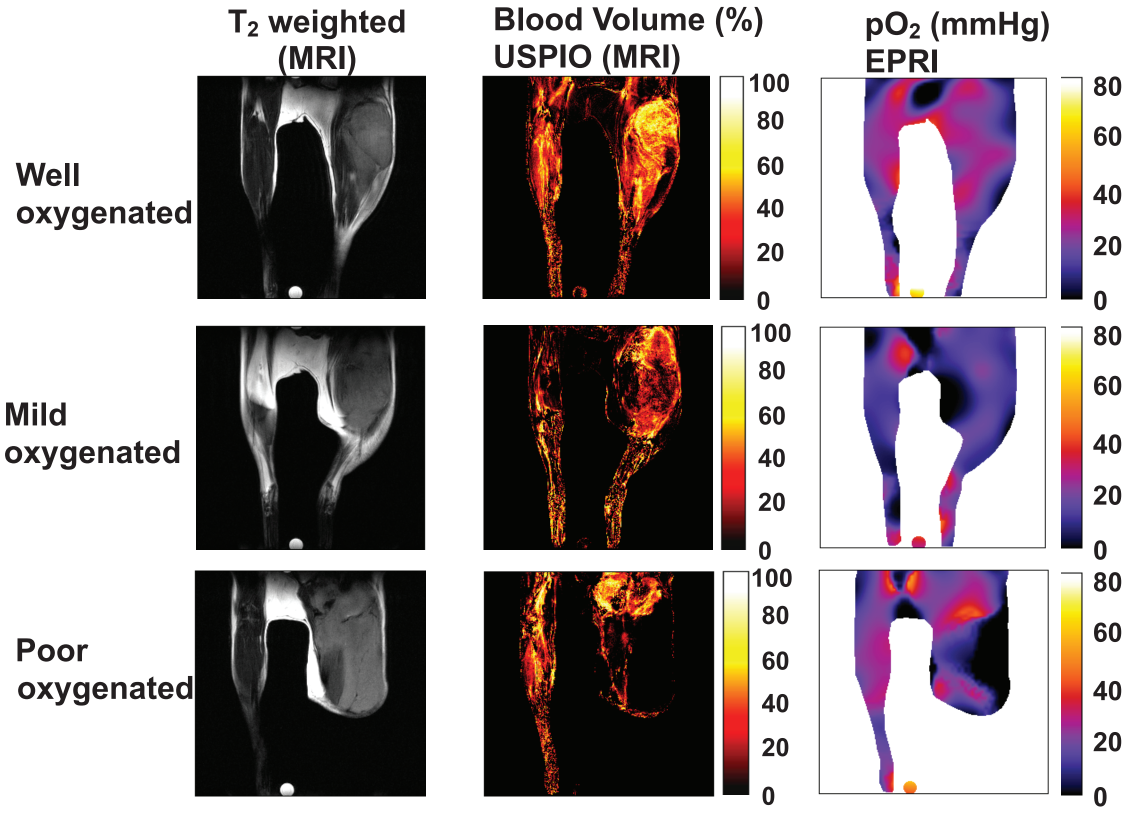

Figure 20. Co-registered MRI and EPR images. The left column shows coronal slices (5 mm) through the SCC tumor-bearing and normal mouse legs from T_2-weighted MRI. The middle column shows the blood volume (%) image (MRI) derived from difference in GE image intensities before and after the injection of USPIO (ultra small super paramagnetic iron oxide). The right column shows the pO_2 map obtained from multi-gradient EPR SPI. The trend in the oxygenation (modulated by allowing the mouse to breathe gases with different percentage of oxygen, 95%, 10% and 20%) is faithfully revealed by the EPR oxygen maps and shows a parallel to the blood-volume images from MRI.

2004). In addition, it will be good to be able to select a slice of anatomy in the desired location so that the imaging time will come down further by an order of magnitude since one has to deal with only 2D encoding. Frequency selective excitation in presence of a gradient for slice selection is not yet feasible in time domain EPR. However, it may be possible to profile the Zeeman field in such a way that only a narrow slice of the object is excited by the pulse. We have done some preliminary work using supplementay Zeeman coils that is able to restrict the resonance band width to a 5 mm thick slice in the direction of the Zeeman axis in time-domain EPRI. Further work is needed in designing special supplementary colis for precise slice selection. It has also been shown that modulated gradients will enable slices of object to be encoded in CW EPRI (Sato-Akaba, Abe, Fujii et al. 2008).

Acknowledgements

This research was supported by the Intramural Research Program of the NIH, Center for Cancer Research, National Cancer Institute. The review presented here covers mostly our EPR imaging development efforts that started more than a decade ago. Generous gift of the TAM derivatives by Klaes Golman of Nycomed Innovations, Malmö, Sweden, and many helpful discussions with Golman, Ardenkjaer-Larsen, and many others at Nycomed innovations are gratefully acknowledged. Several colleagues and collaborators have substantially contributed to these developments and continue to provide valuable support. We would like to place on record our sincere gratitude to all these, including James Mitchell, Angelo Russo, Ram Murugesan, John Cook, Nallathamby Devasahayam, Gadisetti Chandramouli, Periannan Kuppusamy, Rolf Tschudin, Janusz Koscielniak, Jeeva Munasinghe, Tom Pohida, Salem Ghadi, Randall Pursely, Mobae Afeworki, Ken Yamada, MS Moni, Chandrika Baby, Ken-ichiro Matsumoto, Atsuko Matsumoto, Fuminori Hyodo, Emi Hyodo, Shingo Matsumoto, Anastasia Sowers, Frank Harrington, Aravalluvan Thirumaran, Christopher Dharmaraj

and many others. We have tried, as far as possible, to provide adequate reference to the works of others in this field.

Disclosure

The authors report no conflicts of interest.

References

Alecci, M., Dellapenna, S., Sotgui, A. et al. 1992. Electron-Paramagnetic Resonance Spectrometer for 3-Dimensional Invivo Imaging at Very Low-Frequency. *Rev. Sci. Instrum.*, 63:4263–70.

Alecci, M., Brivati, J.A., Placidi, G. et al. 1998. A submicrosecond resonator and receiver system for pulsed magnetic resonance with large samples. *J. Magn. Reson.*, 132:162–6.

Ardenkjaer-Larsen, J.H., Laursen, I., Leunbach, I. et al. 1998. EPR and DNP properties of certain novel single electron contrast agents intended for oximetric imaging. *J. Magn. Reson.*, 133:1–12.

Balcom, B., Beyea, S.D., Green, D.P. et al. 1996a. Single-Point Ramped Imaging with *T*1 Enhancement (SPRITE). *J. Magn. Reson.*, *A*, 123:131–4.

Balcom, S.D., Beyea, S.D., Green, D.P. et al. 1996b. Imaging of heterogeneous materials with a turbo spin echo single-point imaging technique. *J. Magn Reson.*, 144:255–65.

Berliner, L.J. and Fujii, H. 1985. Magnetic resonance imaging of biological specimens by electron paramagnetic resonance of nitroxide spin labels. *Science*, 227:517–9.

Berliner, L.J. (ed). 2003. *In vivo* EPR. (ESR.) New York: Kluwer Academic.

Bloch, F., Hansen, W.W. and Packard, H.E. 1946. Nuclear Induction. *Phys. Rev.*, 69:127–31.

Bracewell, R.N. 1994. Two dimensional imaging New York: Prentice Hall.

Brivati, J.A., Stevens, A.D. and Symons, M.C.R. 1991. A radiofrequency ESR. spectrometer for *in vivo* imaging. *J. Magn. Reson.*, 92:480–9.

Brownell, G.L., Budinger, T.F., Lauterbur, P.C. et al. 1982. Positron Tomography and Nuclear Magnetic-Resonance Imaging. *Science*, 215:619–26.

Callaghan, P.T. 1993. Principles of Nuclear Magnetic Resonance Microscopy Oxford: Oxford University Press.

Chzhan, M., Kuppusamy, P., Samouilov, A. et al. 1999. A tunable reentrant resonator with transverse orientation of electric field for *in vivo* EPR. spectroscopy. *J. Magn. Reson.*, 137:373–8.

Czoch, R., Duchiewicz, J., Francik, A. et al. 1983. EPR. spectrometer with rapid scan. *Meas. Automatic. Contr.*, 29:41–3.

Dadok, J. and Sprecher, R.F. 1974. Correlation Nmr-Spectroscopy. *J. Magn. Reson.*, 13:243–8.

Deng, Y.M., He, G.L., Petryakov, S. et al. 2004. Fast EPR. imaging at 300 MHz using spinning magnetic field gradients. *J. Magn. Reson.*, 168:220–7.

Devasahayam, N., Subramanian, S., Murugesan, R. et al. 2000. Parallel coil resonators for time-domain radiofrequency electron paramagnetic resonance imaging of biological objects. *J. Magn. Reson.*, 142:168–76.

Devasahayam, N., Murugesan, R., Matsumoto, K. et al. 2004. Tailored sinc pulses for uniform excitation and artifact-free radio frequency time-domain EPR. imaging168:110–7.

Eaton, G.R., Eaton, S.S. and Maltempo, M.M. 1989. 3 Approaches to Spectral Spatial Epr Imaging. *Appl. Radiat. Isotopes*, 40:1227–31.

Eaton, G.R., Eaton, S.E. and Ohno, K. (eds.). 1991. EPR. imaging and *in vivo* EPR. Boca Raton: CRC Press.

Eaton, S.S. and Eaton, G.R. 1986. EPR. imaging. *Spectroscopy*, 1:32–5.

Eaton, S.S., Maltempo, M.M., Stemp, E.D.A. et al. 1987. Three-diemnsional EPR imaging with one spectral and two spatial diemnsions. *Chem. Phys. Lett.*, 142:567–9.

Eaton, S.S., Eaton, G.R. and Berliner, L.J. (eds.). 2005a. Biomedical EPR. Part B. New York: Springer.

Eaton, S.S., Eaton, G.R. and Berliner, L.J. (eds.). 2005b. Biomedical EPR. Part A New York: Springer.

Emid, S. and Creyghton, J.H.N. 1985. High-resolution NMR. imaging in solids. *Physica B.*, 128B.:81–3.

Emsley, J.W., Feeney, J. and L, H. 1965. High Resolution Nuclear Magnetic Resonance Spectroscopy Oxford: Pergamon Press.

Ernst, R.R. 1970. Magnetic resonance with stochastic excitation. *J. Magn. Reson.*, 3:10–27.

Ewert, U. and Herrling, T. 1986. Spectrally resolved EPR tomography with stationary gradient. *Chem. Phys. Lett.*, 129:516–20.

Field, L.D., Sternhill, S. and Sternhill, L.S. 1989. Analytical NMR. New York: John Wiley and Son.

Freeman, R. 1998 in Progress in Nuclear Magnetic Resonance Spectroscopy (eds.). Emsley, J.W., Feeney, J. and Sutcliffe, L.H. 59–106 Oxford: Pergamon.

Froncisz, W. and Hyde, J.S. 1982. The Loop-Gap Resonator—a New Microwave Lumped Circuit Electron-Spin-Resonance Sample Structure. *J. Magn. Reson.*, 47:515–21.

Froncisz, W., Oles, T. and Hyde, J.S. 1989. Murine L-Band Esr Loop Gap Resonator. *J. Magn. Reson.*, 82:109–14.

Gallez, B., Debuyst, R., Dejehet, F. et al. 1998. Small particles of fusinite and carbohydrate chars coated with aqueous soluble polymers: Preparation and applications for *in vivo* EPR oximetry. *Magn. Reson. Med.*, 40:152–9.

Gatenby, R.A. and Gillies, R.J. 2004. Why do cancers have high aerobic glycolysis? *Nat. Rev. Cancer*, 4:891–9.

Golman, K., Leunbach, I., Ardenkjaer-Larsen, J.H. et al. 1998. Overhauser-enhanced MR imaging (OMRI). *Acta. Radiol.*, 39:10–17.

Golman, K., Petersson, J.S., Ardenkjaer-Larsen, J.H. et al. 2000. Dynamic *in vivo* oxymetry using Overhauser enhanced MR imaging. *J. Magn. Reson. Imaging*, 12:929–38.

Golman, K., Leunbach, I., Petersson, J.S. et al. 2002. Overhauser-enhanced MRI. *Acad. Radiol.*, 9:S104–S8.

Gravina, S. and Cory, D.G. 1994. Sensitivity and resolution of constant-time imaging. *J. Magn. Reson. B.*, 104:53–61.

Grucker, D. 2000. Oxymetry by magnetic resonance: applications to animal biology and medicine. *Prog. Nucl. Mag. Res. Spectr.*, 36:241–70.

Gupta, R.K., Ferretti, J.A. and Becker, E.D. 1974. Rapid Scan Fourier-Transform Nmr-Spectroscopy. *J. Magn. Reson.*, 13:275–90.

Haacke, E.M., Brown, R.W., Thompson, M.R. et al. 1999. Magnetic Resonance Imaging: Physical Principles and Sequence Design New York: John Wiley and Sons.

Halpern, H.J., Spencer, D.P., van Polen, J. et al. 1989. Imaging radio frequency electron-spin-resonance spectrometer with high resolution and sensitivity for *in vivo* measurements. *Rev. Sci. Instrum.*, 60:1040–50.

Halse, M., Rioux, J., Romanzetti, S. et al. 2004. Centric scan SPRITE magnetic resonance imaging: optimization of SNR, resolution, and relaxation time mapping. *J. magn. Reson.*, 169:102–17.

He, G., Deng, Y., Li, H. et al. 2002. Proton MRI Co-Imaging of Living Mice with EPR. Functional Imaging of Free Radicals. *Proc. Intl. Soc. Magn. Reson. Med.*, 10.

Hirata, H., Walczak, T. and Swartz, H.M. 1997. An improved inductive coupler for suppressing a shift in the resonance frequency of electron paramagnetic resonance resonators. *Rev. Sci. Instrum.*, 68:3187–91.

Hirata, H. and Luo, Z.W. 2001. Stability analysis and design of automatic frequency control system for *in vivo* EPR spectroscopy. *Magn. Reson. Med.*, 46:1209–15.

Hirata, H., Walczak, T. and Swartz, H.M. 2001. Characteristics of an electronically tunable surface-coil-type resonator for L-band electron paramagnetic resonance spectroscopy. *Rev. Sci. Instrum.*, 72:2839–41.

Hirata, H. and Fujii, H. 2007. Automatic matching control circuit based on phase-sensitive detection for *in vivo* CW-EPR. spectroscopy. *Meas. Sci. Tech.*, 18:N.27–N.31.

Hyde, J.S., Froncisz, W. and Oles, T. 1989. Multipurpose Loop Gap Resonator. *J. Magn. Reson.*, 82:223–30.

Hyde, J.S., Mchaourab, H.S., Camenisch, T.G. et al. 1998. Electron paramagnetic resonance detection by time-locked subsampling. *Rev. Sci. Instrum.*, 69:2622–8.

Ilangovan, G., Zweier, J.L. and Kuppusamy, P. 1999. Preparation and characterization of a highly sensitive EPR oximetry probe for biological application. *Free. Rad. Biol. Med.*, 27(Suppl. 1):S106.

Ilangovan, G., Zweier, J.L. and Kuppusamy, P. 2000a. Electrochemical preparation and EPR studies of lithium phthalocyanine: Evaluation of the nucleation and growth mechanism and evidence for potential-dependent phase formation. *J. Phys. Chem. B.*, 104:4047–59.

Ilangovan, G., Zweier, J.L. and Kuppusamy, P. 2000b. Electrochemical preparation and EPR studies of lithium phthalocyanine. Part 2: Particle-size-dependent line broadening by molecular oxygen and its implications as an oximetry probe. *J. Phys. Chem. B.*, 104:9404–10.

Ilangovan, G., Li, H.Q., Zweier, J.L. et al. 2001. Electrochemical preparation and EPR studies of lithium phthalocyanine. 3. Measurements of oxygen concentration in tissues and biochemical reactions. *J. Phys. Chem. B.*, 105:5323–30.

Ilangovan, G., Li, H.Q., Zweier, J.L. et al. 2002. *In vivo* measurement of tumor redox environment using EPR. spectroscopy. *Mol. Cell. Biochem.*, 234:393–8.

Ingram, D.J.E. 1955. SpectroScopy at Radio and Microwave Frequencies London: Butterworths.

Jiang, J.J., Nakashima, T., Liu, K.J. et al. 1996. Measurement of pO_2 in liver using EPR. oximetry. *J. Appl. Physiol.*, 80:552–8.

Joshi, J.P., Ballard, J.R., Rinard, J.A. et al. 2005. Rapid-scan EPR with triangular scans and Fourier deconvolution to recover the slow-scan spectrum. *J. Magn. Reson.*, 175:44–51.

Kak, A.C. and Slaney, M. 1988. Principles of computerized tomographic imaging New York: IEEE Press.

Kevan, L. and Bowman, M.K. (eds.). 1990. Modern pulsed and continuous-wave electron spin resonance New York: John Wiley and Sons.

Koscielniak, J., Devasahayam, N., Moni, M.S. et al. 2000. 300 MHz continuous wave electron paramagnetic resonance spectrometer for small animal *in vivo* imaging. *Rev. Sci. Instrum.*, 71:4273–81.

Krishna, M.C., English, S., Yamada, K. et al. 2002. Overhauser enhanced magnetic resonance imaging for tumor oximetry: Coregistration of tumor anatomy and tissue oxygen concentration. *P. Natl. Acad. Sci. U.S.A.*, 99:2216–21.

Kuppusamy, P., Chzhan, M., Vij, K. et al. 1994. 3-Dimensional spectral spatial EPR imaging of free-radicals in the heart—a technique for imaging tissue metabolism and oxygenation. *Proc. Natl. Acad. Sci. U.S.A.*, 91:3388–92.

Kuppusamy, P., Chzhan, M., Wang, P.H. et al. 1996a. 3D gated EPR. imaging of the beating heart: Time-resolved measurements of free radical distribution during cardiac contractile cycle. *Magn. Reson. Med.*, 35:323–8.

Kuppusamy, P., Chzhan, M., Wang, P.H. et al. 1996b. Three-dimensional gated EPR imaging of the beating heart: Time-resolved measurements of free radical distribution during the cardiac contractile cycle. *Magn. Reson. Med.*, 35:323–8.

Lauterbur, P.C. 1973. Image Formation by Induced Local Interactions: Examples Employing Nuclear Magnetic Resonance. *Nature*, 242:190–1.

Lauterbur, P.C. and Lai, C.M. 1980. Zeugmatography by Reconstruction from Projections. *Ieee. Trans. Nucl. Sci.*, 27:1227–31.

Lauterbur, P.C., Levin, D.N. and Marr, R.B. 1984. Theory and Simulation of Nmr Spectroscopic Imaging and Field Plotting by Projection Reconstruction Involving an Intrinsic Frequency Dimension. *J. Magn. Reson.*, 59:536–41.

Lauterbur, P.C. 1986. Nmr Imaging in Biomedicine. *Cell. Biophys.*, 9:211–4.

Liu, K.J., Gast, P., Moussavi, M. et al. 1993. Lithium phthalocyanine: a probe for electron paramagnetic resonance oximetry in viable biologic systems. *Proc. Natl. Acad. Sci. U.S.A.*, 90:5438–42.

Lurie, D.J., Bussell, D.M., Bell, L.H. et al. 1988. Proton-electron double magnetic resonance imaging of free radical solutions. *J. Magn. Reson.*, 76:366–70.

Mailer, C., Robinson, B.H., Willimas, B.B. et al. 2003. Spectral Fitting: The Extraction of Crucial Information from a Spectrum and a Spectral Image. *Magn. Reson. Med.*, 49:1175–80.

Mailer, C., Subramanian, V.S., Pelizzari, C.A. et al. 2006. Spin Echo Spectroscopic Electron Paramagnetic Resonance Imaging. *Magn. Reson. Med.*, 55:904–12.

Maltempo, M.M. 1986. Differentiation of spectral and spatial components in EPR imaging using 2-D image reconstruction algorithms. *J. Magn. Reson.*, 69:156–63.

Maltempo, M.M., Eaton, S.S. and Eaton, G.R. 1987. Spectral-spatial two dimensional EPR imaging. *J. Magn. Reson.*, 72:449–55.

Maltempo, M.M., Eaton, S.S. and Eaton, G.R. 1988. Reconstruction of spectral-spatial two dimensional images from incomplete sets of projections without prior knowledge of the component spectra. *J. Magn. Reson.*, 77:75–83.

Maresch, G.G., Mehring, M. and Emid, S. 1986. High resolution ESR. imaging. *Physica.*, 138B.:261–3.

Marr, R.B., Chen, C-N and Lauterbur, P.C. (eds.). 1981. On two approaches to 3D reconstruction in NMR. zeugmatography New York/Berlin: Springer-Verlag.

Matsumoto, K., Thirumaran, A., Chandrika, B. et al. 2003. *In vivo* electron paramagnetic resonance oxymetry: Comparison of continuous wave and pulsed techniques. *Free Rad. Biol. Med.*, 35(Supp.1):462.

Matsumoto, K., Chandrika, B., Lohman, JAB. et al. 2003. Application of continuous-wave EPR spectral-spatial image reconstruction techniques for *in vivo* oxymetry: Comaprison of projection reconstruction and constant-time modalities. *Magn. Reson. Med.*, 50:865–74.

Matsumoto, S., Nagai, M., Yamada, K. et al. 2005. A composite resonator assembly suitable for EPR/NMR coregistration imaging. *Conc. Magn. Reson.*, 25B:1–11.

Matsumoto, S., Hyodo, F., Subramanian, S. et al. 2008. Low-field paramagnetic resonance imaging of tumor oxygenation and glycolytic activity in mice. *J. Clin. Invest.*, 118:1965–73.

Mitchell, D.G. and Cohen, M.S. 2003. MRI Principles London: WA Saunders.

Moonen, C.T.W., Bandettini, P.A., Aquirre, G.K. et al. 1999. Functional MRI New York: Springer Verlag.

Murugesan, R., Afeworki, M., Cook, J.A. et al. 1998. A broadband pulsed radio frequency electron paramagnetic resonance spectrometer for biological applications. *Rev. Sci. Instrum.*, 69:1869–76.

Natterer, F. 1986. The mathematics of computerized tomography Chichester: Wiley.

Ogawa, S., Tank, D.W., Menon, R. et al. 1992a. Intrinsic signal changes accompanying sensory stimulation—functional brain mapping with magnetic resonance imaging. *Proc. Natl. Acad. Sci. U.S.A.*, 89:5951–5.

Ohno, K. and Watanabe, M. 2000. Electron paramagnetic resonance imaging using magnetic-field-gradient spinning. *J. Magn. Reson.*, 143:274–9.

Ono, M., Ogata, T., Hsieh, K.C. et al. 1986. L-Band Electron-Spin-Resonance Spectrometer Using a Loop-Gap Resonator for *Invivo* Analysis. *Chem. Lett.*, 491–4.

Panagiotelis, I., Nicholson, I. and Hutchison, J.M.S. 2001. Electron spin relaxation time measurements using radiofrequency longitudinally detected ESR and application in oximetry. *J. Magn. Reson.*, 149:74–84.

Pandian, R.P., Parinandi, N.L., Ilangovan, G. et al. 2003. Novel particulate spin probe for targeted determination of oxygen in cells and tissues. *Free rad. biol. Med.*, 35:1138–48.

Pandian, R.P., Kim, Y.I., Woodward, P.M. et al. 2006. The open molecular framework of paramagnetic lithium octabutoxynaphthalocyanine: implications for the detection of oxygen and nitric oxide using EPR spectroscopy. *J. Mater. Chem.*, 16:3609–18.

Pfenninger, S., Forrer, J., Schweiger, A. et al. 1988. Bridged Loop Gap Resonator—a Resonant Structure for Pulsed Electron-Spin-Resonance Transparent to High-Frequency Radiation. *Rev. Sci. Instrum.*, 59:752–60.

Poole, C.P. 1997. Electron Spin Resonance: A Comprehensive Treatise on Experimental Techniques New York: John Wiley and Sons.

Purcell, E.H., Torrey, H.C. and Pound, R.V. 1946. Resonance absorption by nuclear moments in solid. *Phys. Rev.*, 69:37–8.

Pursley, R., Kakareka, J., Salem, G. et al. 2003. Stochastic excitation and Hadamard correlation spectroscopy with bandwidth extension in RF FT-EPR. *J. Magn. Reson.*, 162:35–45.

Pursley, R.H., Salem, H., Pohida, T.J. et al. 2005. Direct detection and time-locked subsampling applied to pulsed electron paramagnetic resonance imaging. *Rev. Sci. Instrum.*, 76:1–6.

Pursley, R.H., Salem, G., Devasahayam, N. et al. 2006. Integration of digital signal processing technologies with pulsed electron paramagnetic resonance imaging. *J. Magn. Reson.*, 178:220–7.

Quine, R.W., Rinard, G.W., Eaton, S.S. et al. 2002. A pulsed and continuous wave 250 MHz electron paramagnetic resonance spectrometer. *Conc. Magn. Reson.* (*Magn. Reson. Engineer*), 15:59–91.

Ramachandran, G.N. and Lakshminarayanan, A.V. 1971. Three-dimensional reconstruction from radiographs and electron-micrographs:application of convolutions instead of Fourier transforms. *Proc. Natl. Acad. Sci. U.S.A.*, 68:2236–40.

Rinard, G.A., Quine, R.W. and Eaton, G.R. 2000. An L-band crossed-loop (bimodal) EPR resonator. *J. Magn. Reson.*, 144:85–8.

Rubinson, K.A., Cook, J.A., Mitchell, J.B. et al. 1998. FT-EPR. with a nonresonant probe: Use of a truncated coaxial line. *J. Magn. Reson.*, 132:255–9.

Sakamoto, Y., Hirata, H. and Ono, M. 1995. Design of a Multicoupled Loop-Gap Resonator Used for Pulsed Electron-Paramagnetic-Resonance Measurements. *IEEET Microw. Theory*, 43:1840–7.

Sato-Akaba, H., Abe, H., Fujii, H. et al. 2008. Slice-Selective Images of Free Radicals in Mice With Modulated Field Gradient Electron Paramagnetic Resonance (EPR) Imaging. *Magn. Reson. Med.*, 59:885–90.

Schweiger, A. and Jeschke, G. 2001. Principles of Pulse Electron Paramagnetic Resonance Oxford: Oxford University Press.

Shepp, L.A. and Logan, B.F. 1974. The Fourier reconstruction of a head section. *IEEE. Trans. Nucl. Sci.*, NS-21:21–43.

Shepp, L.A. 1980. Computerized tomography and nuclear magnetic resonance. *J. Comp. Assist. Tomogr.*, 4:94–107.

Stoner, J.W., Szymanski, D., Eaton, S.S. et al. 2004. Direct-detected rapid-scan EPR at 250 MHz. *J. Magn. Reson.*, 170:127–35.

Subramanian, S., Murugesan, R., Devasahayam, N. et al. 1999. High-speed data acquisition system and receiver configurations for time-domain radiofrequency electron paramagnetic resonance spectroscopy and imaging. *J. Magn. Reson.*, 137:379–88.

Subramanian, S., Yamada, K., Irie, A. et al. 2002a. Noninvasive *in vivo* oximetric imaging by radiofrequency FT EPR. *Magn. Reson. Med.*, 47:1001–8.

Subramanian, S., Devasahayam, N., Murugesan, R. et al. 2002b. Single-point (constant-time) imaging in radiofrequency Fourier transform electron paramagnetic resonance. *Magn. Reson. Med.*, 48:370–9.

Subramanian, S., Matsumoto, K.I., Mitchell, J.B. et al. 2004. Radio frequency continuous-wave and time-domain EPR imaging and Overhauser-enhanced magnetic resonance imaging of small animals: instrumental developments and comparison of relative merits for functional imaging. *Nmr in Biomedicine*, 17:263–94.

Subramanian, S., Koscielniak, J., Devasahayam, N. et al. 2007. A new strategy for fast radiofrequency CW EPR imaging: Direct detection with rapid scan and rotating gradients. *J. Magn. Reson.*, 186:212–9.

Swartz, H.M. and Walczak, T. 1998. Developing *in vivo* EPR oximetry for clinical use. *Adv. Exp. Med. Biol.*, 454:243–52.

Weil, J.A., Bolton, J.R. and Wetz, J.E. 1994. Electron Paramagnetic Resonance: Elementary theory and practical applications New York: Wiley-Interscience.

Yamada, K., Murugesan, R., Devasahayam, N. et al. 2002. Evaluation and comparison of pulsed and continuous wave radio frequency electron paramagnetic resonance techniques for *in vivo* detection and imaging of free radicals. *J. Magn. Reson.*, 154:287–97.

Yong, L., Harbridge, J., Quine, R.W. et al. 2001. Electron spin relaxation of triarylmethyl radicals in fluid solution. *J. Magn. Reson.*, 152:156–61.

Zavoisky, E. 1945. Spin-magnetic resonance in paramagnetics. *J. Phys. E.*, 9:245–9.

Ziessow, D. and Bluemich, B. 1974. Hadamard-NMR-spektroskopie. Ber. Bunsenges. *Phys. Chem.*, 11:1168–79.

Zweier, J.L., Wang, P.H. and Kuppusamy, P. 1995. Direct Measurement of Nitric-Oxide Generation in the Ischemic Heart Using Electron-Paramagnetic-Resonance Spectroscopy. *J. Biol. Chem.*, 270:304–7.